Optics & Laser Technology 192 (2025) 114058

Contents lists available at ScienceDirect

Optics and Laser Technology

journal homepage: www.elsevier.com/locate/optlastec

Latest achievements in metalenses for advanced imaging applications

B. Patrizi [a,b,*], A. Santonocito [a,c], G. Toci [a]

[a] CNR-INO, Consiglio Nazionale delle Ricerche, Istituto Nazionale di Ottica, Via Madonna del Piano 10, 50019 Sesto Fiorentino, FI, Italy
[b] LENS, European Laboratory for Non Linear Spectroscopy, Via Nello Carrara 1, 50019 Sesto Fiorentino, FI, Italy
[c] Dipartimento di Chimica, Università di Pisa, Via Giuseppe Moruzzi 13, Pisa 56124, Italy

ARTICLE INFO

Keywords:
Metalenses
Metalens design fundamentals, Chromatic aberration
Hyperspectral imaging
Multispectral imaging
Polarimetric imaging

ABSTRACT

Metalens technology is rapidly advancing the frontiers of optical imaging by enabling flat, lightweight, and multifunctional alternatives to conventional refractive elements. Recent progress in improving efficiency, chromatic dispersion control, and scalable fabrication has positioned metalenses as pivotal components of next-generation optical platforms. In the first part of this review, we survey key developments in metalens design that address long-standing challenges in optics, including chromatic aberration, high-numerical-aperture focusing, and correction of higher-order aberrations such as spherical aberration and astigmatism. We then explore their integration into advanced imaging modalities, specifically multispectral, hyperspectral, and polarimetric systems, highlighting their role in enhancing imaging quality and operational capability. Finally, we discuss emerging applications in passive depth sensing, edge-enhanced imaging, and hybrid computational architectures, where deep neural networks are leveraged to restore broadband metalens-acquired images. Collectively, these innovations mark a paradigm shift in imaging science, with far-reaching implications for consumer optics, biomedical instrumentation, and industrial metrology, where compactness, performance, and integrability are paramount.

1. Introduction

Metasurfaces have emerged as a groundbreaking technology with the potential to revolutionize light manipulation. Optical metamaterials are artificially structured materials at nanoscale with unconventional properties at optical frequencies [1–4]. Optical metamaterials have emerged as one of the most exciting and disruptive topics in the field of optics, with an exponential growth in the last five years, thanks to combined advances in nanofabrication, computational electromagnetic design and simulations, and characterization tools. Metasurfaces (and among them, metalenses) can be considered a special class of optical metamaterials, featuring quasi-2D geometries. Unlike traditional optical components that rely on gradual phase changes and bulky designs, metasurfaces consist of ultra-thin, planar structures covered with arrays of nanoscale structures called *meta*-atoms. These structures are capable of controlling light with unprecedented precision [5,6], enabling the focusing, steering, or shaping of the incident wavefronts with unprecedented control and minimal aberration. On the other hand, traditional optical systems, particularly those requiring high resolution and complex aberration correction, often rely on multiple lens elements stacked together.

Optical metasurfaces present several benefits for new generation optical technologies such as the miniaturization of optical components [7], the implementation of advanced functions (e.g. polarization discrimination, spectral de-multiplexing), the integration of multiple functions in a single device, and the fast and real-time tunability of the optical response [7–10].

As research and development in this area continue to advance, metasurfaces are poised to play a crucial role in the next generation of optical devices, driving innovations that could transform industries and enhance everyday life. The sharp reduction in size makes metalenses particularly attractive for applications where space and weight are critical, such as in smartphone cameras, augmented reality (AR) headsets, and satellite imaging systems [11,12].

Nevertheless, metalenses can also be affected by limitations such as chromatic aberration and low optical efficiency. In this context, recent progress in metalens design has been directed toward addressing these intrinsic limitations. Chromatic aberration is one of the main limitations in optical imaging; it arises when distinct wavelengths of light focus at different points, causing color fringing or blurred edges in the image, a

* Corresponding author..
E-mail address: barbara.patrizi@ino.cnr.it (B. Patrizi).

https://doi.org/10.1016/j.optlastec.2025.114058
Received 29 May 2025; Received in revised form 12 September 2025; Accepted 2 October 2025
Available online 17 October 2025

widely recognized limitation that also affects conventional lenses. To overcome this limitation, researchers have developed achromatic metalenses, which are designed to focus multiple wavelengths of light at the same point, significantly improving image quality across the visible spectrum [13]. Moreover, metalenses demonstrated strong potential for imaging systems with sub-wavelength resolution [14], a capability particularly important for applications such as microscopy and nanoscale lithography, where high resolution is paramount. Another key direction of research involves the development of multifunctional and tunable metalenses. These metalenses can dynamically adjust their focusing properties in response to external stimuli, such as voltage, temperature, or mechanical strain, allowing real-time control of the optical properties [7,15], enabling for adaptive optics that adjust instantly to different imaging scenarios without the need for mechanical movement.

The ongoing improvements in fabrication methods are making the incorporation of metalenses into commercial devices increasingly viable. Conventionally, metalens fabrication has depended on advanced nanofabrication techniques such as electron-beam lithography (EBL), which offer high precision but lack scalability for mass production. Recent efforts have focused on developing scalable manufacturing processes, such as nanoimprint lithography (NIL) and Deep UV (DUV) lithography, which could enable the widespread adoption of metalenses in consumer electronics and other technological fields.

In the first part of this review, we summarize recent literature highlighting the significant progress of metalenses in overcoming long-standing optical challenges inherent to traditional lenses such as chromatic aberration, high numerical apertures (NAs), and correction of higher-order aberrations, such as spherical aberration and astigmatism. Alongside this, we also examine the recent literature on zoom metalenses to gain deeper insight into the tuning strategies and their limitations. Indeed, we consider the progress in this specific field capable of profoundly influencing the evolution of optics applications.

In the second part we report on multispectral, hyperspectral and polarimetric imaging and how the advancements in metalens technology has the capability to revolutionize imaging by making systems more compact, efficient, and capable of integrating advanced optical and computational functions to extract and process complex information from light in real time. At the end of this section, we discuss the current limitations and challenges that must be addressed for this technology to be integrated into existing imaging systems and implemented on a large scale.

2. Improving light manipulation through metalenses

2.1. Fundamentals of metalenses design

Metasurfaces are arrays of metallic or dielectric *meta*-atoms, placed on a sub-wavelength periodic lattice, whose geometrical parameters (e.g. height, width, orientation) are suitably modulated across the metasurface area. Each *meta*-atom is dimensioned to provide the desired phase or amplitude variation on the emerging electromagnetic field.

From the point of view of the operating principle, a metasurface can be explained by means of the Huygens' Principle (see Fig. 1). Each point at the interface (i.e. each *meta*-atom) acts as a spherical wavelet source, and the new wavefront originates from the interference of the various wavelets.

The geometrical parameters of the individual scatterers are modulated across the aperture of the metasurface to obtain the desired spatially varying wavefront modulation. The required phase imparted by *meta*-atoms should span the interval 0–2 π in order to obtain a full control of the overall phase delay distribution determined by the metasurface. It is worth noticing that the spacing of the *meta*-atoms is usually smaller than λ in order to prevent the formation of diffracted modes.

For accurate operation of the metalens, each *meta*-atom should ideally operate independently, with minimal interaction (or coupling) with its neighbours. This independence ensures that the phase shift provided by each *meta*-atom is exactly as designed, without being influenced by neighbouring structures. This can be achieved by spacing the *meta*-atoms adequately or by carefully designing their shapes to minimize coupling effects. Taking into account this, achieving a specific optical function involves the following three logical steps:

- the definition of the overall phase difference map $\varphi_{target}(x,y)$ that the metasurface is expected to impart to the emerging wavefront, that determines the metasurface optical function; for design reasons, it is useful to fold the phase map in the 0-2π interval as $\widetilde{\varphi}_{target}(x,y) = (\varphi_{target}(x,y) mod 2\pi)$
- the individuation of a set of *meta*-atoms capable to impart a phase shift between 0 and 2π to the wavefront, by changing parameters (indicated as $\boldsymbol{P}$) such as the size, shape or orientation, $\varphi(\boldsymbol{P})$ so that $0 \leq \varphi(\boldsymbol{P}) \leq 2\pi$;
- the definition of the distribution of *meta*-atoms on the metasurface surface, able to realize the desired phase delay map by the proper spatial distribution of the parameter $\boldsymbol{P}_{target}(x,y)$, i.e. $\widetilde{\varphi}_{target}(x,y) = \varphi(\boldsymbol{P}_{target}(x,y))$.

For instance, in the simple case of focusing/defocusing of a plane wave at the wavelength λ (corresponding to an angular frequency $\omega = 2\pi c/\lambda$) incident normally to the metalens, the phase delay that the metalens has to impart to the incoming wavefront is calculated using the following lens equation (Eqn 1):

$$\boldsymbol{\varphi}(\boldsymbol{r},\boldsymbol{\omega}) = -\frac{\omega}{\boldsymbol{c}}\left(\sqrt{\boldsymbol{r}^2+\boldsymbol{f}^2}-\boldsymbol{f}\right) \quad (1)$$

where f is the focal length of the lens, $r = \sqrt{x^2+y^2}$, is the distance from the optical axis, x and y are the coordinates on the metasurface measured from the lens axis. The negative sign denotes a converging

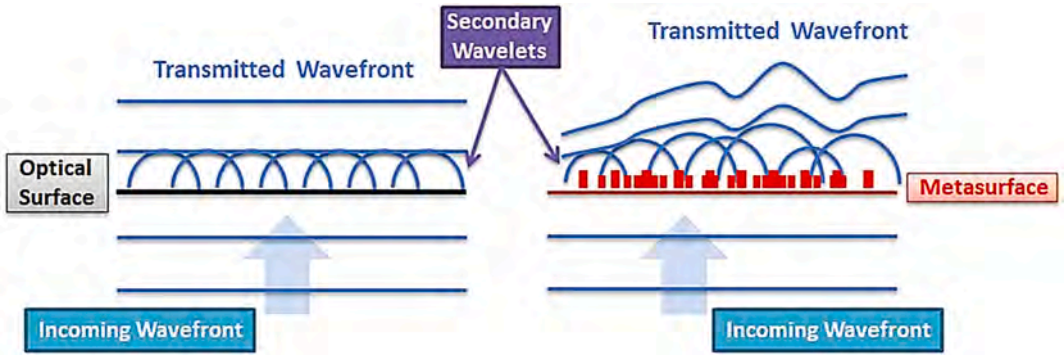

Fig. 1. Application of the Huygens' Principle to a flat, uniform optical surface (left), and to a metasurface (right).

(focusing) phase profile; for a diverging (defocusing) phase profile the sign is positive. The relation above describes a simple lens operating on axis at a single wavelength, and with a reduced numerical aperture (NA).

Metasurfaces operate mainly through three phase modulation mechanisms as described by Pan *et al.* [16], i.e.:

- phase shift of resonance;
- propagation phase;
- geometric phase.

The *Phase shift of resonance* exploits the resonant scattering of metallic elements (nanoantennas) due to Localized Plasmon Resonance (LPR). In the simplest case, a linear antenna of length L_0 is resonant with an incoming vacuum wavelength λ_0 when its length is $L_0 \cong \lambda_0/2$. For a perfect conductor the equality for the previous equation holds about exactly, but at optical frequencies the vacuum resonant wavelengths are smaller, and the resonance condition is rather expressed as $L_0 = \lambda_{eff}/2$ where λ_{eff} correspond to the plasmonic oscillation wavelength in the metal, as pointed out by [17]. At resonance, the phase delay between the incident and the scattered wave is $\pi/2$. For $L < L_0$ the phase shift becomes $< \pi/2$ and asymptotically goes to 0, while when $L > L_0$ the phase delay grows up to π [18]. Therefore, adjusting the distribution of antennas lengths on the metasurface it is possible to adjust the phase delay distribution in the interval 0-π.

Full phase coverage of 0-2π can be obtained exploiting more complex architectures, based on Metal-Insulator-Metal (MIM) structures, and supporting the so-called surface-gap plasmon resonances [19,20].

In the *propagation phase* modulation strategy, the *meta*-atoms consist of high aspect ratio elements, such as nanopillars made of high refractive index materials, with heights on the order of the wavelength (H ~ λ), standing on a low refractive index substrate and behaving as waveguides. These elements are arranged on a sub-wavelength spaced lattice and the phase tuning is achieved by an accurate design of the structural parameters. The guided propagation constant (i.e. the effective phase velocity) differs from the free propagation wavenumber of the bulk dielectric material and it can be adjusted by modifying the physical parameters of each unit cell [14,21,22]. For instance, in the simple case of cylindrical pillars, the propagation can be described using the theory of cylindrical dielectric waveguides. The propagation constant β (i.e. the equivalent of the wavenumber for the guided propagation) of propagating modes in a dielectric cylinder with refractive index n_2, radius a, surrounded by a medium with lower refractive index n_1 (e.g. air) depends on the so-called normalized frequency $V = (2\pi a/\lambda)\sqrt{n_2^2 - n_1^2}$

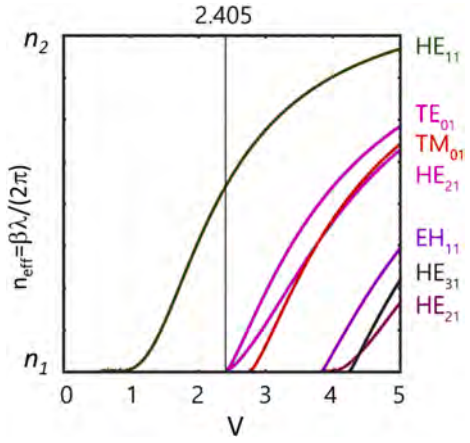

Fig. 2. Effective refractive index n_{eff} associated to the propagation constant β, for various low-order propagation modes in cylindrical waveguides. V is the normalized frequency (see text), n_1 and n_2 are the refractive indexes of the surrounding medium and of the dielectric material of the cylinder respectively.

where λ is the vacuum wavelength (see Fig. 2).

For vanishing V (i.e. $\lambda \gg a$) the effective refractive index approaches n_1 (i.e. that of the surrounding medium), while for increasing V (decreasing λ) the effective refractive index asymptotically approaches n_0 (i.e. that of the dielectric).

The phase delay introduced by an isolated nanopillar with propagation constant β and height H is then (Eqn 2):

$$\Delta\varphi = (2\pi n_1/\lambda - \beta)H \tag{2}$$

Adjusting the radius a of the pillars with constant height H provides thus a convenient way to adjust the phase delay. It must be noticed that the pillar supports a single propagation mode as long as $V \leq 2.405$, i.e. $\lambda \geq (2\pi a/2.405)\sqrt{n_2^2 - n_1^2}$. For shorter wavelengths ($V > 2.405$), higher order modes with different propagation constants become allowed resulting in more complex dependence of the phase delay. When the pillars are arranged in closely spaced arrays, coupling effects between the individual pillars can affect the effective propagation constants, but these effects are weak as long as the difference between n_2 and n_1 is large, and they can be accurately modelled with currently available numerical simulation packages. Finally, we note that if the cross section shapes of the pillars are not symmetric upon 90° rotation around their vertical axis (e.g. pillars with rectangular or elliptical cross section), the pillars will feature different propagation constants depending on the polarization of the propagating radiation (i.e. birefringence), that can be adjusted by acting on the shape of the cross section. This property can be exploited to obtain polarization-dependent response (see for instance [23–25]).

The *geometric phase control* method can be used when the phase delay introduced by the individual *meta*-atoms depends on the polarization of the incoming radiation (i.e. they are birefringent). This can be achieved by using shapes that lack rotational symmetry along the propagation direction (e.g. pillars with rectangular, elliptical or more complex shapes). This is called Pancharatnam-Berry (PB) phase shift [14].

This method can be conveniently applied when the incoming wave is circularly polarized.

To illustrate this method, we will make use of the Jones matrices [26]. The transmittance (or reflectance) of the *meta*-atom is assumed to be different for two perpendicular polarization states, parallel respectively to the ordinary (o) and extraordinary (e) axis of the *meta*-atom. The complex transmittance (or reflectance) coefficients are designed t_o and t_e respectively. When the ordinary and extraordinary axes are aligned with the x and y axes of the reference frame, the corresponding Jones matrix is (Eqn 3):

$$\boldsymbol{T} = \begin{pmatrix} t_o & 0 \\ 0 & t_e \end{pmatrix} \tag{3}$$

When the *meta*-atom is rotated around the z axis by an angle θ, the T matrix is transformed as (Eqn 4):

$$\begin{aligned} \boldsymbol{T}(\theta) &= \begin{pmatrix} \cos(\theta) & -\sin(\theta) \\ \sin(\theta) & \cos(\theta) \end{pmatrix} \begin{pmatrix} t_o & 0 \\ 0 & t_e \end{pmatrix} \begin{pmatrix} \cos(\theta) & \sin(\theta) \\ -\sin(\theta) & \cos(\theta) \end{pmatrix} \\ &= \begin{pmatrix} t_o\cos^2(\theta) + t_e\sin^2(\theta) & (t_o - t_e)\cos(\theta)\sin(\theta) \\ (t_o - t_e)\cos(\theta)\sin(\theta) & t_e\cos^2(\theta) + t_o\sin^2(\theta) \end{pmatrix} \end{aligned} \tag{4}$$

The incoming wavefront is assumed to be circularly polarized (CP), either right-handed (RCP) or left handed (LCP), and propagating along the z axis. The Jones representation of the electric field is (Eqn 5):

$$\boldsymbol{E_{in}} = E_0 \begin{pmatrix} 1 \\ \pm i \end{pmatrix} \tag{5}$$

(the + and – signs refer to LCP and RCP respectively).

The emerging field after transmission is $\boldsymbol{E}\cdot\boldsymbol{T}(\theta)$ that is (Eqn 6):

$$\boldsymbol{E_{out}}(\theta) = E_0\frac{t_o + t_e}{2}\begin{pmatrix} 1 \\ \pm i \end{pmatrix} + E_0\frac{t_o - t_e}{2} exp(\pm i2\theta)\begin{pmatrix} 1 \\ \mp i \end{pmatrix} \tag{6}$$

The equation above shows that, upon transmission, part of the field (the first addend) emerges with the same handedness of the incoming polarization; part of the field (the second addend) emerges with opposite handedness, and with a phase delay (i.e. $exp(\pm i2\theta)$) that depends on the geometrical rotation angle θ of the *meta*-atom. By rotating the *meta*-atom with θ going from 0 to π, the phase delay covers the full range 0-2π. It must be noticed that such a phase control method relies only on the orientation of the *meta*-atoms and it can be applied to both metallic and dielectric *meta*-atoms.

In a metasurface exploiting the PB phase control method, only a single shape of *meta*-atom is needed to obtain the full 0-2π phase delay. On the other hand, the *meta*-atoms do not necessarily need to be identical to each other, so that the PB method can also be associated with the other methods exposed above, e.g. by combining rotation with the modulation of size of metallic antennas, or with the variation of the shape/size of dielectric pillars, that result in a variation of the transmission (or reflection) coefficients t_o and t_e. This approach has been dubbed composite phase modulation method by some authors [27–31], and it provides further degrees of freedom in the design, allowing better control on aspects such as the manipulation of different polarization states or the control of the phase delay over a broad spectral range.

2.2. Aberrations and wide Field-of-View performance

The realization of efficient lenses for large field-of-view (FOV) wideband imaging applications require more sophisticated designs and realization, in order to take into account three main problems, i.e. monochromatic aberrations, chromatic aberrations for broadband imaging, high NA.

On axis spherical aberration can be avoided by properly defining the phase map imparted by the metalens. For instance, the parabolic phase distribution of Eqn 1 provides inherently free spherical aberration focusing for a plane wave (object located at infinite) [32–38]. This phase profile cannot be realized exactly with traditional lenses based on spherical surfaces, except for small NA, so it requires the implementation of aspherical surfaces [39]. Conversely, the proper phase profile can be implemented in metalenses in the design and fabrication process because the phase profile of the metalenses can be defined on a point-by-point basis by acting on the *meta*-atom distribution. It must be noticed that the phase profile needed for coma-free imaging of an object located at finite distance (i.e. with a spherical incoming wavefront) does not necessarily correspond to the one defined in Eqn 1, but this can be easily calculated with simple algebraic methods [39].

An evaluation of the capability of a lens (or a metalens) to provide aberration-free focusing from a source (located either at infinite or at finite distance) can be obtained considering the size of the actual Point Spread Function (PSF) intensity distribution with respect to the ideal one (set by the diffraction limit). For an ideal lens the PSF corresponds to the Airy pattern whose main lobe diameter at FWHM is $d_{Airy} = 1.03\lambda f/D = 0.502\lambda/\mathrm{NA}$ (where f is the focal length, D is the diameter of the lens aperture and NA is the numerical aperture) [40]. A real lens matching this performance is defined as diffraction limited. Note that for NA > 0.5 the size of the diffraction-limited PSF becomes smaller than the wavelength λ (sub-wavelength resolution).

A closely related performance indicator is the Strehl ratio, that is the ratio of the peak intensity of a measured PSF with respect to the peak intensity of a perfect diffraction-limited PSF with the same aperture and focal length [41]. The closer the Strehl ratio to 1, the better the performance of the lens.

In a milestone paper published in 2016, Khorasaninejad *et al.* demonstrated a diffraction-limited imaging system with sub-wavelength resolution using a metalens with a diameter of 2 mm and NA of 0.8 [14]. This metalens is composed of TiO_2 *meta*-atoms, which are transparent across the visible spectrum. In order to effectively modulate the wavefront of the incoming light, these *meta*-atoms are oriented in accordance with the PB phase. The metalens was tested on axis at the wavelengths of 660, 532, and 405 nm. Under 532 nm light, the metalens produced a focal spot with a full width at half maximum (FWHM) of 375 nm (that is only 5 % larger than the corresponding diffraction limited spot); a similar near-diffraction limited performance was obtained at 660 nm and at 405 nm, with Strehl ratios of ~ 0.77. For demonstration purposes, in the paper above the performance of the metalens was compared with that of a commercial, state-of-the-art objective lens (100 × Nikon CFI 60, NA = 0.8), which in the same test set-up yielded a spot with FWHM of 600 nm (i.e. about twice the diffraction limit) at 532 nm. It could be noticed that the benchmark lens is designed for water immersion operation, while the test was carried out in air, resulting in a sub-optimized performance.

Among the various optical aberrations, coma plays a critical role in image quality. Coma aberration can be considered as the off-axis manifestation of spherical aberration, and it is influenced by the angle at which light enters the lens. When light strikes the lens at an off-axis angle, it fails to focus correctly on the image plane, creating distorted focal spots resembling a comet (coma). This distortion hampers the lens's capacity to capture wide FOV images, limiting the sharp, image-able area to small sections around the center of the image plane. To overcome this limitation, aplanatic metalenses, which correct both spherical and coma aberrations simultaneously, are highly desired. Ideally, a flat metalens capable of focusing light at any incident angle θ_i should implement a phase profile explicitly dependent on θ_i [27] as shown in (Eqn 7):

$$\boldsymbol{\varphi}(\boldsymbol{r},\lambda) = -\frac{\omega}{\boldsymbol{c}}\left(\boldsymbol{r}\boldsymbol{sin}\theta_i\sqrt{(\boldsymbol{r}-\boldsymbol{f}\boldsymbol{tan}\theta_i)^2+\boldsymbol{f}^2}-\frac{\boldsymbol{f}}{\boldsymbol{cos}\theta_i}\right) \tag{7}$$

Traditional metalens designs often apply a phase shift that does not change with the angle of incoming light. While this simplifies the design, it also means that the lens's ability to focus light properly decreases as the angle of incidence increases, leading to aberrations and a reduced FOV. This limitation restricts the metalens's performance, particularly in applications that require a wide FOV. To overcome this limitation particular designs have been developed to effectively address different imaging needs, ranging from basic lens corrections to complex, high-quality imaging systems. Some common architectures i.e. aberration corrected singlets, the Chevalier Landscape lens and the aplanatic doublet have emerged [16] and are depicted in Fig. 3.

In the Chevalier Landscape Lens architecture (Fig. 3b), a small aperture acts as aperture stop to separate the normally and obliquely incident rays which are then focused by different parts of the metalens. This design allows the different regions of the metalens to be separately optimized, enabling simultaneous correction of both on-axis and off-axis aberrations. This principle has been demonstrated in two recent studies: Engelberg *et al.* [42] reported a wide-angle near-infrared (NIR) metalens with a 30° FOV, while Shalaginov *et al.* [43], presented a fisheye lens in the medium wave Infrared (MWIR) with 170° FOV. Aplanatic performance can also be achieved using a double-metalens configuration, known as the doublet technique (Fig. 3c), in which an additional optical component is placed at the front focal plane of the lens to correct coma and spherical aberrations. In this case the first metalens corrects the coma aberration and the second acts as a spherical aberration-corrected lens. This approach was implemented by Arbabi *et al.* [44] where a miniature camera lens is introduced, that corrected both spherical and coma aberrations using a metalens doublet. Combinations of these architectures have also been explored. Groever *et. al* [45] proposed a Chevalier architecture where a metalens is placed at the entrance pupil acting as correcting plate. This metalens doublet has a numerical aperture of 0.44, a focal length of 342.5 μm, and a FOV of 50° and it is capable of near-diffraction-limited monochromatic imaging along the focal plane at a wavelength of 532 nm.

Table 1 resumes the characteristics of metalenses for wide FOV focusing, mainly developed for imaging applications, from visible to

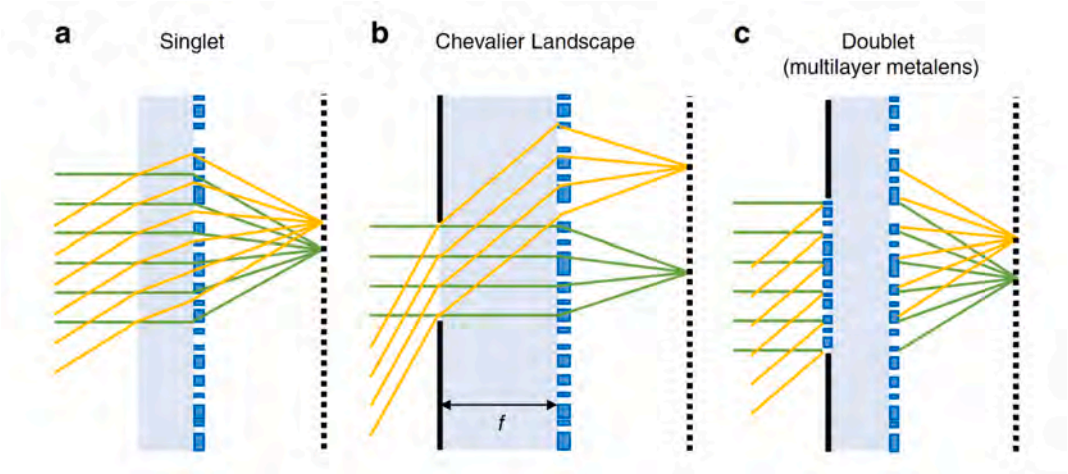

Fig. 3. Common architectures for reducing aberration. **a.** Singlet aplanatic metalens. **b.** Chevalier Landscape metalens. **c.** Doublet aplanatic metalens. The figure has been reproduced from reference [16] under Creative Commons CC BY license.

Table 1
Characteristics of selected examples of focusing metalenses with large Field of View, from visible to LWIR.

Operation wavelength	Focusing efficiency	FOV (full angle)	Entrance aperture	(PSF width) /(diffr. limit)	Strehl ratio	Metasurface type/Architecture	Refs
532 nm	N/A	50°	0.3 mm	<1.05	N/A	TiO_2 on fused silica; doublet/Chevalier architecture	[45]
532 nm	N/A	93°	5.7 mm	<1.1	N/A	Silicon Nitride on SiO_2	[46]
532 nm	95 %	160°	3.1x1.7 mm	<1.4		Silicon Nitride on SiO_2, coupled with spatial light modulator	[47]
830 nm	>60 %	120°	11 mm	<1.12	NA	Silicon on sapphire pillars; dual layer architecture (focusing element and angle sorting filter)	[48]
532 nm	3.5 %	180°	2 mm	3	N/A	Crystalline Si on Sapphire, aplanatic singlet	[49]
632.8 nm	N/A	160°	40 μm	~1.2	N/A	Apertures on Au film	[50]
850 nm	70 %	60°	0.8 mm	N/A	~0.9	Amorphous Si on fused silica; doublet	[44]
940 nm	N/A	178°	1 mm	1.1*	N/A	Streamline profiles, Si curved fins on silicon-on-sapphire wafer, Chevalier architecture	[51]
5.2 μm	32–45 %	170°	1 mm	N/A	>0.8	CaF_2 nanopillars on CaF_2 substrate, Chevalier architecture	[43]
10 μm	N/A	80°	10 mm	N/A	N/A	Si nanopillars on Si, Chevalier architecture, air spacer	[52]
10.6 μm	60 %	140°	10 mm		~0.85	Si nanopillars on Si, Chevalier architecture, ZnSe spacer	[53]
10.6 μm	60 %	100°	6 mm		~1 (on axis), ~0.5 (off axis)	Si nanopillars on Si, Chevalier architecture, air spacer	[53]
10.6 μm	N/A	178°	12.7 mm	N/A	N/A	Streamline profiles, Si curved fins on Si, Chevalier architecture	[51]
8—14 μm	79 %	46°	15.2 mm	2	N/A	Diffractive structure on silicon	[54]

long wave infrared (LWIR). Large FOVs, exceeding 90°, were obtained in all the regions of spectrum under consideration, with large (>50 %) focusing efficiencies. The table also reports key performance indicators such as the focusing efficiency, the size of the PSF (relative to the diffraction limit) and the Strehl ratio, extracted from the relevant papers. The realizations in the visible and in the LWIR feature also pupil aperture from several mm to more than 1 cm, which improve light collection efficiency.

2.3. *High numerical aperture and achromatic metalenses*

Another major challenge in optical design is efficiency, particularly in terms of light throughput and focusing power. Recent advancements have led to the creation of metalenses with high NA, which use materials with high refractive indices and optimized nanostructures to ensure that a greater proportion of the incident light is focused correctly, reducing losses and improving image brightness and contrast. This is especially beneficial in applications like microscopy, where high resolution and efficiency are crucial.

It is worth noticing that achieving efficient performance and near diffraction limited operation at high NA eventually results in a constraint on the size of the unit cell of the metalens: indeed, due to the discretization of the phase profile (see Section 2.1) the maximum transverse wavenumber provided by the metalens at the incident wavelength λ is $k_{max} = NA/\lambda$, due to the Nyquist-Shannon sampling theorem. The period p of the unit cell of the metalens must then satisfy the condition $p \leq \lambda/(2NA)$ [45], to prevent that undersampling of the phase profile results in spherical aberration. For NA > 0.5 this criterion becomes more stringent than the simple requirement that $p < \lambda$, needed to prevent the formation of higher order diffraction modes for a normally incident wavefront. Besides, maintaining a high transmission efficiency over a broad range of emerging angles can require a significant effort for the optimization of the *meta*-atom structure.

In the Table 2 are collected the parameters of some recent realizations of high NA metalenses in the visible and in the NIR. Among these, it is worth to underline the striking results described in [55] where is reported a focusing metalens with diffraction limited operation in the visible. It has been realized by DUV lithography on a SiO_2 substrate and exhibits an aperture of 100 mm of diameter. This is the size record to date for metalenses.

Other key innovations in the efficient manipulation of light through metasurfaces has been the development of achromatic metalenses,

Table 2
Examples of functional and design parameters of high NA metalenses.

Operation Wavelength	Focusing Efficiency	NA	Aperture	Metasurface-type/ architecture	Refs
532 nm	50 %	1.1 (oil)	ND	TiO_2 nanofins	[56]
405, 532, 660 nm	86 %, 73 %, 66 %	0.8	2 mm	TiO_2 nanofins on glass	[14]
715 nm	35 %	0.99	600 μm	crystalline Si on a SiO_2 substrate	[57]
500 nm	38 %	0.43	90 μm	Si curved fins on silicon-on-sapphire wafer	[58]
1550 nm	42 %	0.97	400 μm	Si posts on fused silica	[59]
532 nm	67 %	0.98	205 μm	Si rectangular pillars on sapphire	[60]
632.8 nm	60 %	0.32	100 mm	SiO_2 nanopillars on SiO_2 substrate	[55]
10.6 μm	35 %	0.6	12 mm	Si circular pillars on Si substrate	[61]

which are designed to focus light of different wavelengths to the same point. Traditional lenses often suffer from chromatic aberration, where different colours focus at different distances due to the wavelength-dependent refractive index of the material. In conventional optics chromatic aberrations correction is obtained by stacking various lenses made of glasses with different dispersions [62], making the overall system more bulky and costly. On the other hand, metalenses use specially designed *meta*-atoms that provide wavelength-independent phase control, thereby minimizing chromatic aberration using a single, ultrathin lens. By expanding the phase function around a central frequency, it is possible to optimize metalenses minimizing chromatic aberrations and improving performance across the desired wavelength range. In the case of a metalens, expanding the phase profile in a Taylor series around a central wavelength λ_c we obtain (Eqn 8):

$$\boldsymbol{\varphi}(\boldsymbol{r},\omega) = \boldsymbol{\varphi}(\boldsymbol{r},\omega_c) + (\omega-\omega_c)\frac{\partial\boldsymbol{\varphi}(\boldsymbol{r},\omega)}{\partial\omega}\bigg|_{\omega=\omega_c} + \frac{1}{2}(\omega-\omega_c)^2\frac{\partial^2\boldsymbol{\varphi}(\boldsymbol{r},\omega)}{\partial\omega^2}\bigg|_{\omega=\omega_c} + \tag{8}$$

where the latter two terms are the group delay and the group-delay dispersion. As discussed by [13], when the focal length f is frequency independent it must contain no higher-order terms than the linear one [63]. Thus, to realize a perfectly achromatic metalens, working for both broadband pulses and incoherent light, the design should implement a suitable frequency-independent phase pattern $\varphi(r,\omega_c)$, a group delay term independent from wavelength [64], and zero group-delay dispersion and higher-order terms (quadratic and higher order terms in Eqn 3)
.

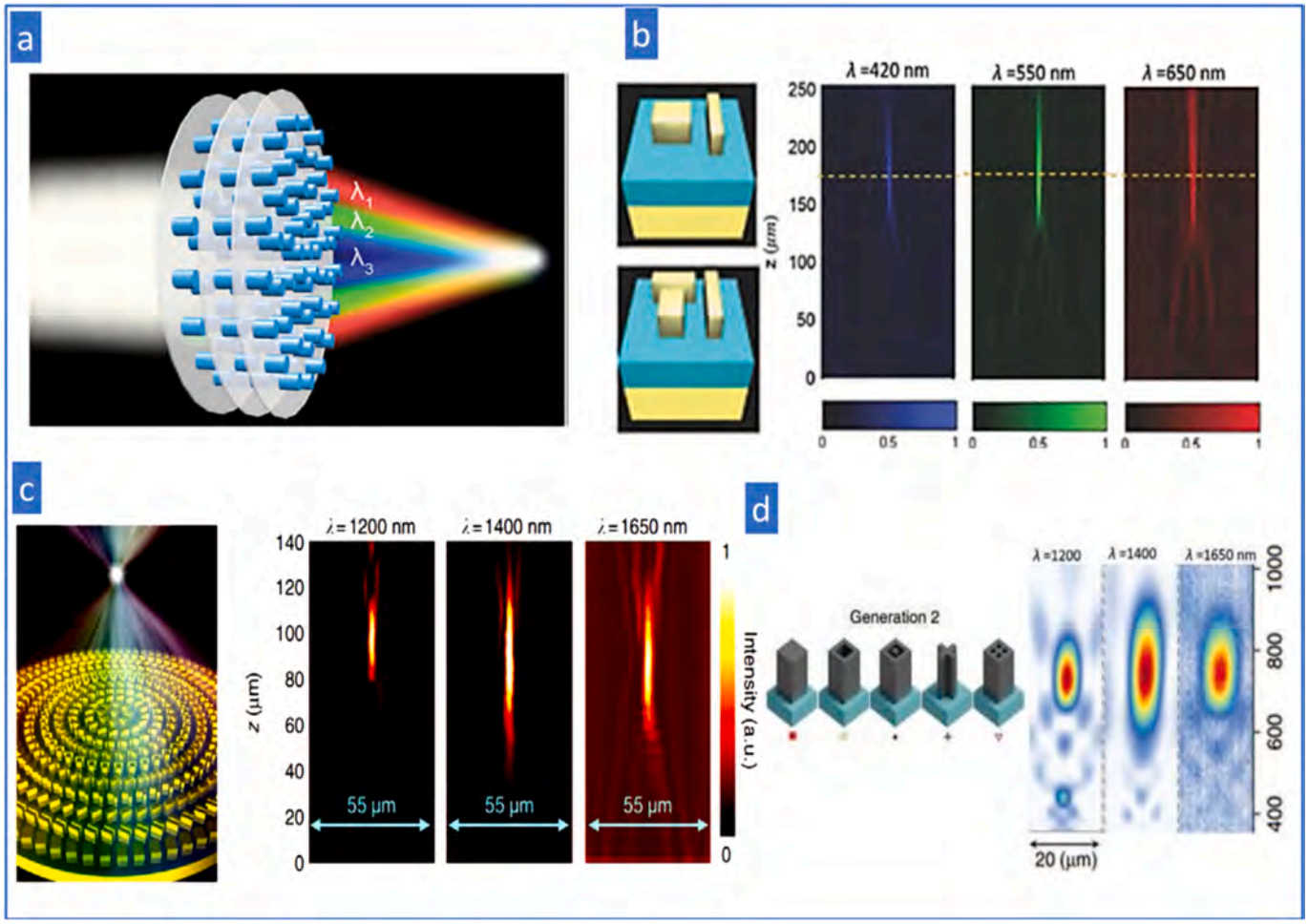

Fig. 4. (a) Multilayer metasurfaces for focusing multiple target wavelengths without chromatic aberration in the visible. Adapted with permission from [65]**; (b)** Aluminium resonator units operating in the visible (400–667 nm). Adapted with permission from [66]**; (c)** Au resonator units, operating in the NIR (680–1200 nm) from [63] **(d)** Amorphous silicon nanopillars for operation in the short wave infrared (SWIR), 1200–1650 nm, from [67] under Creative Commons CC BY license.

Another important consideration is that, under oblique incidence, additional phase compensation is required to manage off-axis dispersion in polychromatic operation [68]. The required phase compensation increases dramatically for increasing distance from the center, making the fabrication of large-area achromatic metalenses particularly challenging. To address this issue, inverse design methods have been utilized to create large-scale aperture metalenses that can operate effectively across a broad range of wavelengths [69]. Dispersive phase compensation can be achieved in several ways (some examples are shown in Fig. 4). Diverse methods to accomplish single layer achromatic metalenses have been reported. The selection of *meta*-atoms design determines the phase modulating mechanism which affects the phase and phase dispersion at each position [67,70]. Applying spatial multiplexing [71–74], cascading [75], or catenary [75], metasurfaces are widely used methods for achromatic focusing. Several examples of metalenses exploiting resonances on plasmonic [63,66,76], or dielectric [13,77–79], *meta*-atoms have been demonstrated. One approach to reducing chromatic aberration in metalenses involves using dielectric resonators with two asymmetrically designed building blocks that create a broad resonance spectrum, effectively eliminating chromatic aberration [77]. In addition, the combination of multiple phase modulation strategies has been demonstrated to yield polarization-insensitive, broadband achromatic metalenses [70]. An effective strategy to address chromatic dispersion is the use of multi-layer stacked metalenses [80] or metalens doublet [81,82] to eliminate chromatic aberration. In multilayer metalenses, composed of amorphous silicon *meta*-atoms embedded in polydimethylsiloxane (PDMS), the operating wavelength range has been shown to broaden with an increase in the number of stacked layers [65], as depicted in Fig. 4a. Demonstrations include a three-layer lens composed of disk-shaped metallic antennas to exploit localized surface plasmonic resonances of three different metallic components achieving polarization-independent focusing in a broad visible light range [83]. The thickness of each layer is tens of or hundreds of nanometer, so the total thickness is only a few micrometers; therefore, multi-layer metalenses can still be realized as ultrathin optical components.

In a paper by F. Presutti *et al.* [64] the problem of achieving simultaneously both large NA and large bandwidth has been thoroughly analyzed, and fundamental limitations were found. They noted that a focusing metalens acts as a delay line, because the parts of the wavefront farther form the axis have to travel a longer free propagation path with respect to those near to the axis, to reach the focal point, and the central part of the metalens has to impart a corresponding delay so that all the parts of the wavefront can arrive at the same time in the focus. The product between achievable time delay and bandwidth is limited in any time-invariant system, that is (see Eqn 9):

$$\Delta T \Delta\omega < \kappa \tag{9}$$

Where κ is an appropriate dimensionless constant; the time delay between the outer part of the metalens and the axis is given by can be put in relation with the NA, resulting in (Eqn 10):

$$\Delta T_{max} = \frac{f}{c}\left(\sqrt{1+(R/f)^2} - 1\right) \tag{10}$$

Where R is the radius of the metalens, f is its focal length, c is the speed of light. Using simple trigonometric relations, R/f can be put in relation with NA and Eqn. (9) and Eqn 10 can be used to set a limit for the waveband achievable with a metalens, namely (Eqn 11):

$$\Delta\omega = \frac{\kappa c\sqrt{1-(NA/n_1)^2}}{f\sqrt{1-\sqrt{1-(NA/n_1)^2}}} \tag{11}$$

Where n_1 is the background refractive index. For a given focal length and immersion medium therefore the maximum achievable bandwidth rapidly decreases with NA, and with the focal length f. A similar result was obtained starting from different considerations in [84]. Values of the characteristic coefficient κ were found to be different for the various phase delay implementation methods. For ultrathin *meta*-atoms (exploiting antennas or localized plasmonic resonances) it is $\kappa = 2$. For *meta*-atoms based on propagation phase delay, it is $\kappa = 2\pi(H/\lambda_c)(n_{max} - n_{min})$ where λ_c is the central operating wavelength, H is the height of the nanopillars, n_{max} and n_{min} are the effective (not bulk) refractive indexes of the resonators (depending on the propagation constant β, see Section 2.1 and Fig. 2); these can be approximated by the index of refraction n_2 of the material constituting the pillars (for n_{max}) and n_1 for the surrounding medium (e.g. air) for n_{min}. The validity of these results and in particular of Eqn 10 has been verified against several metalens realizations. It must be noticed that from a practical point of view equations above do not prevent the attempt of realizing large NA and large bandwidth metalenses, but their spherical and chromatic aberration will rapidly increase for increasing bandwidth.

Besides the fundamental limitations, fabrication issues can challenge the achievement of broadband operation. In a recent study [85], the inherent limitations of achieving achromatic performance in metalenses were thoroughly examined. The study highlighted that while metalenses can theoretically support a broad spectral range, their efficiency is constrained by manufacturing challenges related to the precise control of feature depth and size. Furthermore, the research demonstrated that metalenses can achieve near-diffraction-limited performance, but only at very low Fresnel numbers, meaning they struggle to deliver high focusing power, broadband response, and near-diffraction-limited operation simultaneously. For large metalenses – with apertures spanning several hundreds to thousands of wavelengths – this constraint manifests as a limitation in the achievable NA or as a reduction in resolving power.

Table 3 summarizes the parameters of several recent implementations of broadband and achromatic metalenses in the visible and NIR spectral regions. As shown, many of these examples cover almost the entire visible spectrum, with notable extensions into the NIR. Some designs also feature relatively large clear apertures, ranging from fractions of 1 mm to 1 cm, combined with high NAs, which are crucial for achieving optics with high light collection efficiency. Conversely, other examples have clear apertures only of a few tens of microns in size, positioning them more as proof-of-concept designs rather than viable candidates for practical applications.

Broadband and achromatic metalenses have been developed for the SWIR, MWIR, and LWIR infrared regions, achieving efficient focusing across a wide range of wavelengths. These metalenses feature clear apertures from fractions of a millimeter to over 1 cm, allowing for higher light collection, especially in the LWIR where low $f/\#$ are crucial for detailed imaging. Such designs are essential for applications like thermal imaging, surveillance, and environmental sensing, offering compact and versatile alternatives to traditional optics. Table 4 resumes the parameters of some recent realizations of broadband/achromatic metalenses in these IR regions.

2.4. Zoom metalenses

Another significant advantage in optical technology, leveraging metasurfaces, is the possibility to achieve variable focal lengths in ultrathin and lightweight metalenses. In the so-called zoom metalenses the focal length can be changed under an external stimulus. Unlike traditional zoom lenses, which require complex assemblies of multiple moving lens elements, zoom metalenses can dynamically adjust their focal length through the precise modulation of the phase profile across the lens surface. This adjustment can be achieved without any mechanical movement, often by applying external stimuli such as temperature, voltage or others [7].

Besides of changing the focusing properties of the metalenses themselves, some authors have proposed approaches where the

Table 3
Examples of broad band metalenses in the visible and in the NIR spectral regions. CP denotes operation in circular polarization; NP denotes operation on non-polarized (NP) radiation.

Operation Wavelength	Focusing efficiency	NA	Entrance aperture	Metasurface type/ architecture	Polarization	Refs
400–660 nm	40 %	0.106	25 μm	GaN pillars on Sapphire	CP	[79]
400–660 nm	40 %	0.215	21.6 μm	GaN nanofins on Al_2O_3	CP	[34]
400–760 nm	76 %	0.41	8.64 μm	Si3N4 pillars on glass	NP	[86]
400–1000 nm	64 %	0.1	3.07 mm	Diffractive pattern on polymer	NP	[87]
400–1000 nm	29 %	0.1	10.24 mm	Diffractive pattern on polymer	NP	[87]
420–650 nm	20 %	0.124	41.9 μm	Al nanopillars on SiO_2	CP	[66]
440–660 nm	60 %	0.05	2.5 mm	Diffractive pattern in photoresist	NP	[88]
450–750 nm	22 %	0.18	370 μm	Diffractive pattern in photoresist	NP	[89]
450–1000 nm	12 %	0.3	3.145 mm	Diffractive pattern in photoresist	NP	[90]
450, 550, 650 nm	8.7 %	0.1	212 μm	Al, Ag, Au resonators on SiO_2 stacked structure	NP	[83]
460–700 nm	35 %	0.2	26.4 μm	TiO_2 nanofins	NP	[70]
460–700 nm	32 %	0.2	26.4 μm	TiO_2 nanopillars	NP	[70]
470–670 nm	20 %	0.2	20 μm	TiO_2 nano fins	CP	[13]
470–700 nm	20 %	0.2	25 μm	TiO_2 nanofins	CP	[13]
470, 548, 647 nm	16 %	0.3	1 cm	TiO_2 nanofins on metallic mirror	NP	[91]
650–1000 nm	78 %	0.24	30 μm	TiO_2 pillars on glass	NP	[92]
640–1200 nm	70 %	0.12	20 μm	TiO_2 “fishnet” structure on SiO_2	NP	[93]

Table 4
Examples of broad band metalenses in the SWIR, MWIR and LWIR spectral regions. CP denotes operation in circular polarization, NP denotes operation on non-polarized radiation.

Operation Wavelength	Focusing efficiency	NA	Entrance aperture	Metasurface type/ architecture	Polarization	Refs
1000–1800 nm	68 %	0.27	20 μm	Fused silica	NP	[94]
1180,1400,1680 nm	22 %	0.29	12 0 μm	Si nanopillars on SiO_2 – stacked structure	NP	[65]
1200–1680 nm	12.4 %	0.268	55.6 μm	Au nanorods on SiO_2 layer and Au substrate (reflective)	CP	[63]
1200–1650 nm	32 %	0.13	200 μm	a-Si structured pillars on SiO_2	NP	[67]
1450 – 1590 nm	50 %	0.28	500 μm	Si pillars on SiO_2 layer and Al substrate (reflective)	CP	[78]
1180,1400,1680 nm	22 %	0.29	120 μm	Si nanopillars on SiO_2 – stacked structure	NP	[65]
1300–1700 nm	25 %	0.238	490 μm	Si nanopillars on Sapphire	NP	[19]
3000–4000 nm	52 %	0.35	30 μm	GaAs	NP	[95]
8000–12000 nm	N/A	0.37	15 mm	Diffractive pattern on polymer	NP	[88]

geometrical configuration of a set of static metasurfaces is changed by means of mechanical movements (e.g. translation or rotation), adopting architectures borrowed from traditional optical design. While these approaches sacrifice most of the benefits described above, they can still be convenient because the reduced weight of metalenses with respect to traditional lenses can allow the use of smaller, faster and less powerful mechanical actuators; besides, static metalenses have currently achieved a better maturity than tuneable metalenses. These more conservative approaches will be also discussed below.

Changing the focal length is a fundamental capability for optical systems that can be used either to bring into focus objects at different distances, or (in conjunction with other optical elements) to change the FOV and thus the angular magnification of a lens (zoom objectives). Wei *et al.* [96] propose a metalens doublet working at 1500 nm where the focal length of the doublet changes by varying the relative angle between the metalenses in steps of 10 degrees. The tuning of the doublet focal length has been demonstrated from ± 3 mm to ± 54 mm with a zoom factor of the imaging system varying between 1 and 18. For positive focal lengths, the doublet focusing efficiency has a minimum of 34 % and a maximum of 83 %. It must be considered that mechanical rotation of rigid metasurfaces provides a continuous zoom but sacrifices compactness and speed. Following a similar strategy, a large-area varifocal zoom metalens (1 cm aperture) operating at 1550 nm was demonstrated by Colburn *et al.* [97]. In this system a nonlinear change in focal length is obtained by laterally displacing the regular and inverse cubic metasurfaces with respect to one another (an architecture known as Alvarez lens [98]) with focusing efficiency as high as 57 % and a wide focal length change of more than 6 cm. In this case as well, however, the limitation arises from the need for mechanical components, which constrain both the speed and the compactness of the system.

Paired metalenses have also been employed to achieve tunability of focal length and field of view, in this case by exploiting the polarization of the incident light.

Saragadam and colleagues [99] proposed a system that combines two metalenses, each designed to focus either s- or p-polarized light in the LWIR spectrum. This configuration creates two distinct focal lengths and fields of view: one for foveal vision with s-polarized light (f = 150 mm, 3° FOV) and another for perifoveal vision with p-polarized light (f = 25 mm, 18° FOV). Their experimental configuration use two modes: the first with a linear polarizer to select the system focal length, a second use a single snapshot imaging with a real-time deconvolution algorithm to reconstruct the two images. This polarization-selective designs offer the instantaneous switching without moving parts, but require additional optical elements or computational post-processing.

Another strategy that has been employed to achieve varifocal zoom metalenses is the use of stretchable metasurfaces, where mechanical deformation provides continuous focal tuning [100]. A varifocal broadband graphene metalens on a stretchable PDMS substrate has been demonstrated for multicolor zoom imaging by Wei *et al.* [101]. The tuning is obtained by laterally stretching the lens, obtaining an over 20 % focal length tuning range for red (650 nm), green (550 nm), and blue (450 nm) light. Stretchable varifocal zoom metalenses offer a simple and energy-efficient route to large focal tuning ranges, but their mechanical nature limits speed, stability, and precise phase control.

Another approach to achieve tunability of the focal lengths is the use of phase change materials (PCMs) under temperature external stimulus [102–104].

The development of a varifocal zoom metalens using PCMs like GSST ($Ge_2Sb_2Se_4Te$) represents a significant innovation in adaptive optics. The ability to dynamically alter the focal length and field of view by simply changing the temperature, and thereby the crystalline phase of the material, introduces a versatile and compact solution for zoom

lenses. Yang *et al.* [102] have also proposed a parfocal zoom doublet of metalenses operating in the MIR based on GSST, which achieved large step zoom ratios, minimal distortion, and diffraction-limited optical quality. The device is composed of two metasurfaces patterned on two mid-IR transparent CaF_2 substrates separated by an air gap. GSST-based zoom metalenses leverage the refractive index contrast between amorphous and crystalline phases to dynamically switch optical functionality as a function of the temperature. In a doublet configuration, the metasurfaces operate as a negative–positive pair in the wide-angle mode and as a positive–negative pair in the telephoto mode, thus achieving parfocal 10 × zoom in the mid-infrared without mechanical motion

Wang *et al.* [103] used a low-loss phase change material i.e. the antimony triselenide (Sb_2Se_3) to create a varifocal metalens operating in the NIR. The metalens is designed with two regions. The inner region (region 1) has a focal length of 41 μm (f_1) when the Sb_2Se_3 is in the amorphous state and in the crystalline state, it does not focus light. The outer region (region 2), focuses light at 123 μm (f_2,) when in the crystalline state, but does not focus light in its amorphous state. The focusing efficiency of f_1 and f_2 are 5.74 % and 2.97 %, respectively. The advantage of using PCMs is the compactness, but the response speed is limited by thermal cycling.

Voltage-tunable zoom metalenses have recently emerged as a promising platform for reconfigurable flat optics, offering dynamic control of focal length and field of view through electrically induced phase modulation [105,106].

Bosch *et al.* [107] very recently proposed electrically actuated varifocal zoom metalenses based a periodic array of rectangular amorphous silicon *meta*-atoms embedded in a Liquid-Crystals (LCs) cell and sandwiched between indium tin oxide-coated silicon dioxide plates. The design approach takes advantage from the strong electro-optical response of LCs to electrically tune the *meta*-atom resonances, allowing real-time modulations with a continuously tunable focal length from 20 to 17 mm with a focus efficiency at 808 nm ranging from 8 to 41 %.

A comparative summary of recent zoom metalens implementations is reported in Table 5. These works highlight the diversity of approaches, spanning mechanical rotation, substrate stretching, thermal phase-change, and electrical tuning. Mechanical doublets [96,97] offer continuous zoom at the expense of compactness and focal tuning speed. Phase-change designs [102,103] achieve compact parfocal zoom, though limited by thermal response. Polarization-based concepts [99] allow instantaneous switching but require additional optics and optical processing. More recent advances explore varifocal zoom electrically controlled LC–metalenses [107], pointing toward more practical, fast, and compact zoom imaging systems. It is therefore necessary to find a trade-off between device footprint, speed, and optical efficiency. In this context, at present, voltage-tunable metalenses offer the most favourable compromise. In our opinion, another external stimulus capable of generating an instantaneous response is the magnetic field, provided that magneto-optical materials responsive even at low magnetic field intensities can be identified. Moreover, this kind of modulation does not need physical contact with the metalens such in the case of electrical modulation. Even if the magnetic field as tuning strategy has not yet found application in this type of devices we note that the technology for generating intense and rapidly modulated magnetic fields on sub-micrometer spatial scale is already available from the magnetic hard disks for data storage, where writing heads can generate field strengths up to about 1 T, switched at GHz bandwidth on spatial scales of the order of 100 nm [108].

3. Advanced imaging with metalenses

3.1. Multispectral and hyperspectral imaging

Spectral imaging refers to a collection of techniques used to capture and analyze data across various wavelengths of the electromagnetic spectrum, beyond the visible light that conventional imaging captures. Unlike standard visible imaging, which typically records data in a single channel (panchromatic) or in three colour channels (red, green, and blue), spectral imaging can capture data in many more channels, spanning ultraviolet, visible, and infrared spectral regions. Spectral imaging techniques are categorized based on the number of spectral bands they capture and their method of data acquisition. Multispectral imaging (MSI) typically measures tens of spectral channels, while hyperspectral imaging (HSI) can record as many as hundreds of contiguous spectral bands, leading to a seamless acquisition across the bands of interest [109]. Fig. 5 depicts is a classical comparison between MSI where images are taken in different spectral bands and collected as *slices*, and HSI, in which images are taken across a significantly higher number of bands thereby generating the so-called *hyperspectral cube* [110].

With regard to the acquisition type with respect to spectral dispersion it is possible to have *Dispersive element-based* hyperspectral imaging, or *Spectral Filters Based* HSI solutions where one or more spectral filters are used to transmit the selected spectral bands of interest. Unlike dispersive element based system, where a beam is usually collimated and then dispersed by a grating or a prism, in this approach the incident radiation is directly focused on a 2D filter: unwanted spectral components are blocked, while the desired wavelengths are transmitted [109]. Finally, *Snapshot-based* HSI enables hypercube data acquisition in a

Table 5
Comparative summary of recent zoom metalens implementations.

Operation Wavelength	Metasurface Type	Tuning Mechanism	Efficiency	Focal Length	Polarization Sensitivity	Response Speed	Compactness	Refs
1550 nm	Two metalenses, silicon nano-cylinders	Mutual rotation	From 34 % to 83 %	From ± 3 to ± 54 mm	No	Low	Low	[96]
1550 nm	Two metalenses, silicon nitride nano-cylinders	Mutual displacing	57 %	6 cm	No	Low	Low	[97]
LWIR	Two metalenses, silicon nanoposts and polarizer	Linear polarizer and real-time deconvolution	~ 65 % (f = 25 mm); ~55 % (f = 150 mm)	150 and 25 mm	Yes	High	Low	[99]
450, 550, 650 nm	Graphene oxide rings on PDMS substrate	Substrate stretching	From 27 % to 28 % as a function of Stretch ratios	Red 212–257 μm Green 252–306 μm Blue 310–376 μm	No	Low	Medium	[101]
5.2 μm	Two Metalenses CaF_2 substrate and GSST *meta*-atoms	PCM	8 % (wide-angle mode) and 14 % (telephoto mode)	1.1 mm (wide angle mode) 10.8 mm (telephoto mode)	No	Low	High	[102]
1550 nm	Glass substrate, Sb_2Se_3 nanopillars	PCM	5.74 % (f1) 2.97 % (f2)	41 μm (f_1) 123 μm (f_2)	No	Low	High	[103]
808 nm	Amorphous silicon *meta*-atoms embedded in LCs	External voltage	From 8 % to 41 %	From 20 to 17 mm	No	High	High	[107]

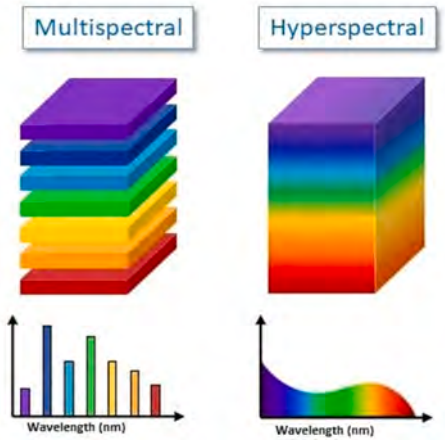

Fig. 5. Comparison Between Multispectral and Hyperspectral Imaging.

single iteration. This approach takes advantage of recent advancements in large format detector arrays, high-speed data transmission, precision optics, and advanced manufacturing techniques. A key advantage is the inherent ability to collect much more light as compared to other implementations, albeit at the cost of increased complexity [109]. An exemplification of these possible acquisition configurations for hyperspectral imagers is depicted in Fig. 6 [111].

Several metalens-based implementations of MSI systems have been developed [112,113]. In reference [112], a metalens platform was designed, fabricated, and tested combining multispectral and polarimetric sorting capabilities. A third device, sharing the features of the latter, has been simulated by the same authors also for orbital angular momentum (OAM) sorting. Fig. 7(**a-d**) illustrates the proposed platform, with each sorting component responsible for spatially de-multiplexing frequency, polarization, and OAM data from an incoming beam. Another strategy for multispectral imaging employs a metasurface that spatially directs incident light into a 2x2 pixel array, with each pixel selectively receiving a specific wavelength band, thereby enabling compact, filter-free spectral discrimination. This method has been demonstrated in the visible spectral region by Miyata *et al.* [114]. This enables the simultaneous capture of light at different wavelengths without the need for filters or other bulky optics. This kind of approach can improve the efficiency and resolution of multispectral imaging systems while reducing their complexity, making them more compact and scalable for real-world applications. Zou *et al.* [113] introduced a highly efficient, inverse-designed pixel-level Bayer colour filter, which is inspired by an earlier filter developed by Lapray [115], which is reported in Fig. 7 (e-g)**.** The metasurface colour filter for RGB imaging shows significant improvements in colour and energy efficiency, with potential versatility for different spectral ranges. It features RGB peak colour efficiencies of 58 % 59 % and 49 %, respectively, with average energy utilization efficiency as high as 84 % over the visible wavelength range. The metasurface is fabricated with dielectric square pillars (SiN on Glass) with potential transpositions in other spectral regions. Filtering principle of this device and the results showing the measured colour collection efficiencies are reported in Fig. 7 (**e-g**).

A recent work shifts from the above concept of selective filtering to an efficient color routing with freeform metasurfaces. Kim *et al.* [116] indeed report a freeform metasurface color router designed for deep submicron pixel image sensors, overcoming the efficiency limits of conventional Bayer color filters. The device consists of a single-layer SiN metasurface (600 nm thickness, 0.6 μm pixel pitch, focal length 0.6 μm) optimized via a fully differentiable topology optimization framework to ensure high efficiency and fabrication robustness. By routing instead of filtering light, the metasurface achieves ~ 85 % average total energy efficiency across the visible band, with experimental routing efficiencies of 33 % (blue, 455 nm), 52 % (green, 530 nm), and 42 % (red, 660 nm).

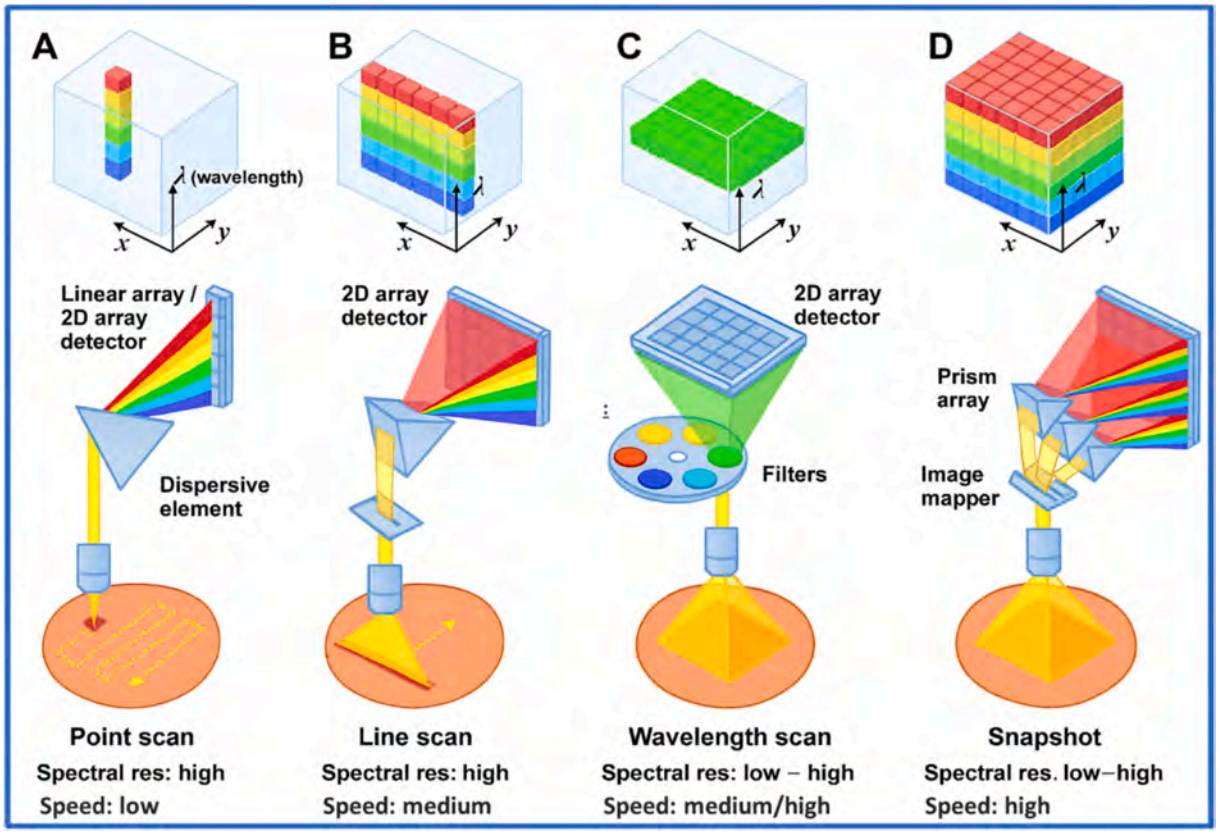

Fig. 6. Hyperspectral Imaging configurations. (A) Point scan. (B) Line scan. (C) Wavelength scan. (D) Snapshot. Reproduced from [111] under Licence CC BY 4.0.

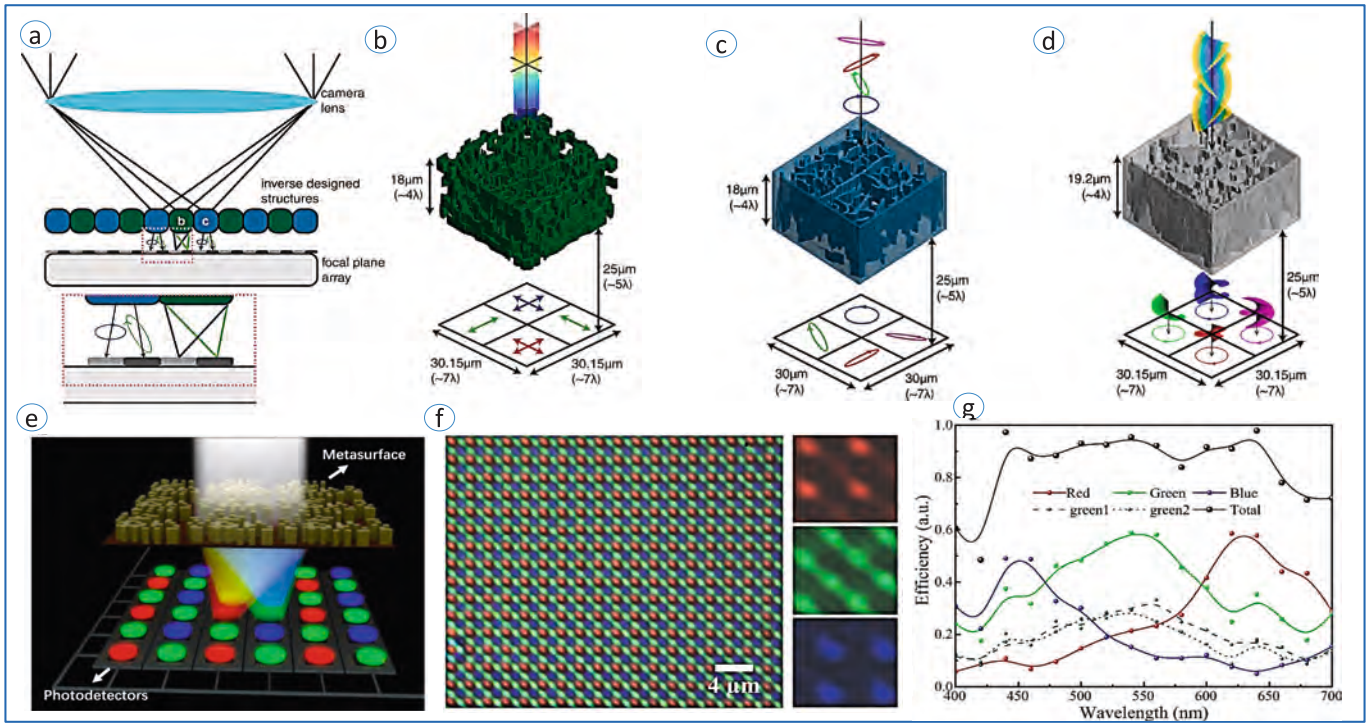

Fig. 7. MSI utilizing metalenses. **(1)** MWIR Multispectral Platform featuring also polarimetric demultiplexing and OAM sorting. (a) 2D cross section schematic of camera with inverse designed scattering elements placed on top of photosensitive elements. Green elements sort by color and blue elements sort by polarization. (b) Rendering of multispectral and linear polarization device that sorts three bands of wavelengths with the middle band further split on polarization. (c) Full Stokes polarimetry device that sorts four analyzer Jones vectors to different quadrants. (d) Angular momentum splitting device that sorts combinations of OAM (l) and spin (s) degrees of freedom. Readapted from [112] under Creative Commons CC BY license **(2)** Metasurface color filter for RGB imaging. (e): filtering principle. (f): measured Image at imaging plane plus 3 colour channels. (g): measured colour collection efficiencies. Readapted from [113] under Creative Commons CC BY license.

Imaging demonstrations with a Macbeth color checker confirm higher SNR and energy utilization (up to 3.5 ×) compared to color-filter arrays. The freeform design exploits multiple eigenmodes to emulate a dispersion-engineered microlens, offering compact ($< (1.2\ \mu m)^3$), fabrication-friendly, and mass-producible solutions for next-generation ultrahigh-resolution image sensors.

One of the first HSI system implemented with metalenses has been reported by Faraji *et al.* [117]. In this system a folded, metasurface-based *push-broom* HSI operating in the NIR (750–850 nm) has been designed, fabricated and tested. The system entails four metasurfaces, where the first one implements a blazed grating dispersing different wavelengths, while the remaining metasurfaces are designed to minimize aberrations and focus the rays on the image plane for the desired wavelengths and angles. Incident light enters in the multiple reflective and transmissive metasurfaces through an input aperture, interacts with the reflective metasurfaces while it is confined inside the substrate by two gold mirrors, and exits through an output aperture incorporating a transmissive metasurface. Different wavelengths are dispersed in the vertical direction (λ), and various input angles are focused to different horizontal points. This result demonstrates the potential of metasurfaces as high-performance diffractive optical elements, offering an effective solution for integrated advanced imaging and smart functions systems.

Lin *et al.,* [118] demonstrated a compact snapshot hyperspectral imager combining a single multi-wavelength off-axis focusing metamirror (MOFM) with a small-data CODE reconstruction. The metamirror is built from anisotropic Al nano-rods (acting as plasmonic *meta*-atoms) deposited on a distributed Bragg reflector (DBR) with chirped layer thicknesses. This DBR provides high reflectivity and supports Tamm resonances, enhancing Q-factors across 500–650 nm spectral range. The geometric phase control imparted to the nano-rods, enables four spatially separated spectral channels in a single shot. These 4-band images are computationally expanded into an 18-band hyperspectral cube using CODE, a convex/deep hybrid algorithm requiring only ~ 18 training examples. Experiments validate high-fidelity reconstruction without filters, and analysis shows scalability of channel number by tuning DBR parameters. This synergy of plasmonic nanorods, DBR metamirror and data-efficient learning paves the way for miniaturized, real-time hyperspectral imaging. We point out that the metalens part of the system, by itself, is only capable to provide information on 4 distinct spectral band, whereas the extrapolation to 18 bands is obtained by means of digital postprocessing (i.e. the CODE algorithm). In principle this can have limitations, in particular when dealing with images whose spectral features are significantly different from that used for the algorithm training.

3.2. Polarimetric imaging

Polarimetric imaging is a type of imaging technique that captures the polarization state of light in addition to its intensity and wavelength. By analysing the polarization of light, polarimetric imaging provides additional information about the object that is not available through conventional imaging methods. Polarimetric imaging has a wide range of applications running the gamut from target detection [119,120] to biomedical diagnostics [121,122], remote sensing [123], defense [124] and astronomy [125] among some of the most relevant fields. Fuelled by aforementioned applications, there is demand for imaging systems able to detect not only light intensity but also its state of polarization (SOP). In conventional polarimetric imaging systems, complex optical components as well as moving parts are generally required, making miniaturization a nontrivial task. [126–128]' With their compact form factor, metasurfaces offer a possible solution to the miniaturization and integration problems [129,130]. In particular, metalenses featuring polarization sensing capabilities have been designed and fabricated [131]. Here we report some of the more significant applications reported in

recent literature. The solution proposed by Ou and co-workers [132] encompasses the design of a broadband polarimetric metaoptic platform in the MWIR wavelength range. This platform features a metalens mapping a specific input SOP state (e.g. s or p polarized beams) to an output beam with a specific topological charge state (BAFOV: Broadband Achromatic Focusing Optical Vortex) and a metalens mapping a specific input SOP state (e.g. s or p polarized beams) to an output beam focusing onto a specific spot in the image plane (BAFS: Broadband Achromatic Focusing Splitter). A schematic illustration of the MWIR polarimetric platform is depicted in Fig. 8.

A further solution proposed by Zuo *et al.* [133] deals with the implementation of a metasurface polarization filter array (MPFA) made of broadband microscale linear polarization filters and dual color circular polarization filters integrated on a CMOS sensor for complete Stokes polarimetry in the visible range. The device is reported in Fig. 9.

A polarization-multiplexed metalens for compact spectral imaging has been proposed by Zhang *et al.* [134]. The authors presented a practical approach for developing chip-integrated full-Stokes polarimetric imaging sensors at visible wavelengths using metasurfaces. This innovation has potential for diverse real-world applications, including autonomous vision systems, industrial quality control, space exploration, and biomedical imaging. The paper presents a compact, polarization-multiplexed spectral imaging system based on a neural-optic co-designed metalens architecture. The metasurface is made of polarization-sensitive silicon nitride (Si_3N_4) nanofins on a silica substrate, optimized to respond differently to orthogonal linear polarization states (0° and 90°). Each nanofin, defined by its length, width, and height (up to 800 nm), acts as a *meta*-atom whose phase and transmittance vary with polarization and wavelength. A key innovation lies in modeling the structure-response mapping using a fully differentiable multi-layer perceptron (MLP), enabling end-to-end joint optimization of the metasurface and the image reconstruction neural network (DI-ResUNet).

The metalens simultaneously encodes spectral and polarization information by generating distinct PSFs under x- and y-polarizations. These encoded signals are captured using a polarization-sensitive camera and decoded to reconstruct high-fidelity hyperspectral images across 420–660 nm spectral range. This approach enables real-time, miniaturized spectral imaging with potential for mobile and wearable platforms.

In a very recent paper Fu *et al.* [135] demonstrated a compact polarimetric stereoscopic imaging system based on a birefringent metalens capable of capturing full-Stokes images with high extinction ratios and transmission efficiency up to 65 % in the range 950–1350 nm. The metalens architecture employs engineered dielectric supercells that perform polarization-selective phase control, focusing six distinct polarization states (H, V, D, A, LCP, RCP) onto spatially separated focal spots. This passive design enables snapshot acquisition of complete polarization information without any moving parts or external filters. The structured imaging output, consisting of six polarization-resolved sub-images, is processed using a Deep Neural Network (DNN) constrained by physical polarization priors, achieving 3D surface reconstruction with sub-millimeter precision. Notably, the integration of circular polarization channels significantly improves surface detail capture and robustness under complex reflectance conditions. This system illustrates the synergy between nanophotonic wavefront engineering and computational vision, offering a scalable and miniaturized solution for real-time 3D reconstruction. Its adaptability makes it suitable for low-light or scattering environments (e.g., haze, underwater), and compatible with portable imaging platforms for applications in AR, biometric identification, and biomedical microscopy.

3.3. Other advanced applications

Certain applications of metalenses extend beyond traditional optical tasks like image capture, and cannot be strictly categorized under multi/hyperspectral or polarimetric imaging. These applications offer advanced optical functionalities that go beyond simple imaging techniques. We report in this section some examples regarding passive distance measurement, edge detection, and a hybrid imaging approach

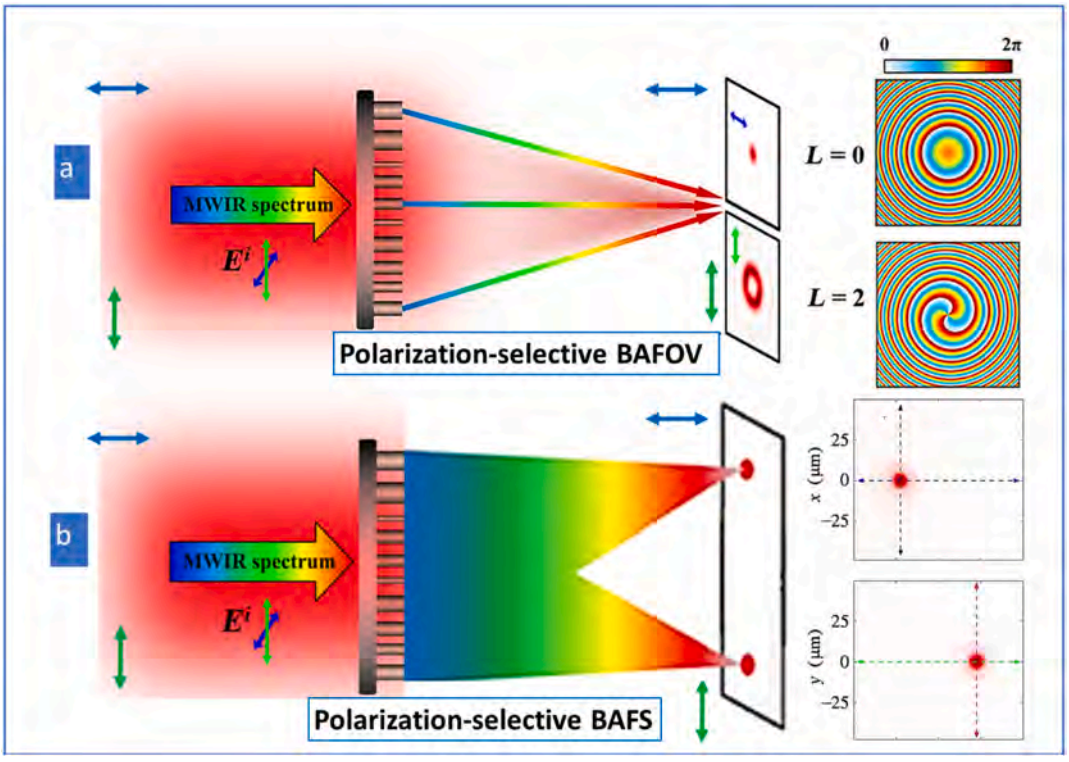

Fig. 8. Illustration of the MWIR polarimetric metaplatform as designed by Ou *et al.* [132] featuring BAFOV **(a)** and BAFS **(b)** metadevices. Both BAFOV and BAFS metadevices have been fabricated in an all-silicon platform and feature high polarization isolation. Readapted under CC BY-NC 4.0 from [132].

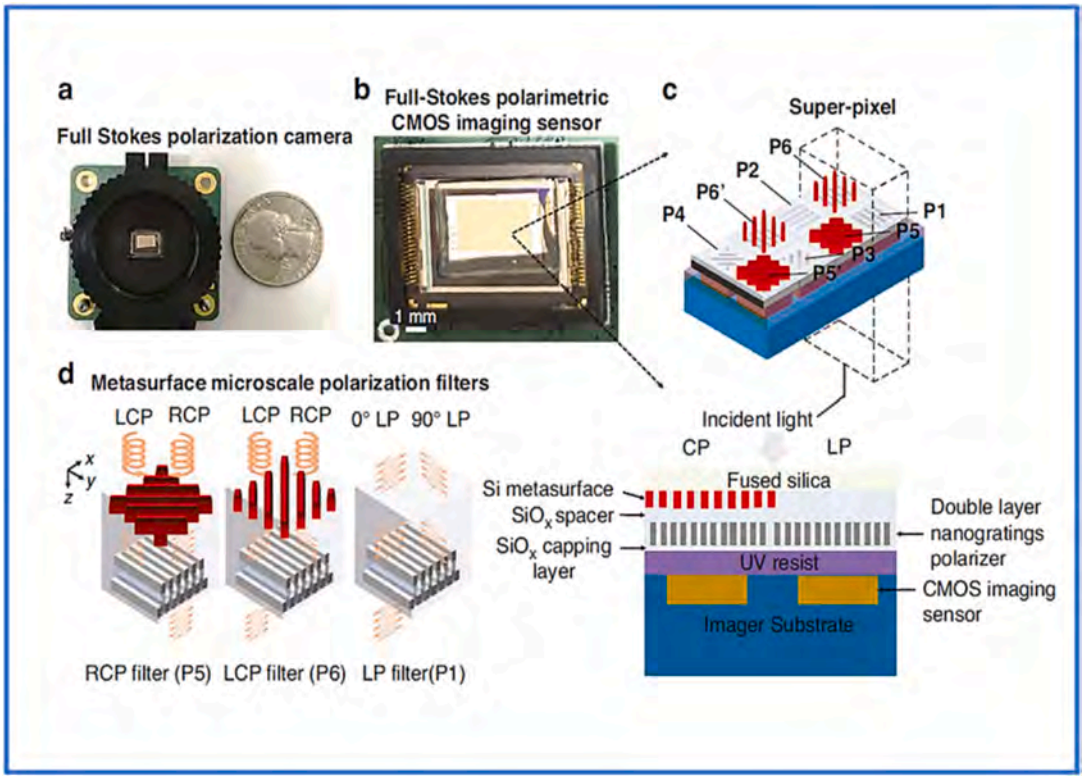

Fig. 9. **(a)** Illustration of the full-stokes polarization camera beside a US quarter dollar coin (lens not attached). **(b)** Image of full Stokes polarimetry CMOS imaging sensor. **(c)** Top: 3D conceptual illustration of a chip integrated full-stokes CMOS polarimetric imaging sensor. P1-P4 denote the linear polarization (LP) filters with transmission axes at 0° 90° 45° 135° respectively. P5,P5′ and P6,P6′ denote chiral metasurface filters transmitting Right-Hand Circular Polarization (RHCP) and Left-Hand Circular Polarization (LHCP) respectively. **(d)** 3D conceptual illustration of a pair of chiral metasurfaces responsible for transmitting RHCP and LHCP light respectively, and a LP filter (P1) reproduced from [128] under licence CC BY-NC 4.0.

addressing the restoration of images acquired with wideband metalens with DNNs. While the realization of these applications does not strictly require optical metasurfaces, their use can nonetheless allow implementing these functions in a very compact way and with a minimum number of components. Metalenses have been applied in advanced imaging techniques, including distance measurements, by utilizing their ability to focus light with high precision [136,137]. In advanced 3D imaging, metalenses are used to generate structured light patterns. When these patterns reflect off objects, the system can analyze the distortions in the reflected light pattern to calculate distances with high-resolution. In this regard, based on jumping spiders vision Guo *et al.* [138] propose a metalens combining two lenses with different focal lengths (Fig. 10). The authors proposed an algorithm to recover the object distance based on the evolution of the camera PSF. The metalens is composed of TiO_2 square pillars on SiO_2 wafer (height = 600 nm, width = 90–190 nm, period = 230 nm, working wavelength at 532 nm). An alternative scheme is proposed by Jin *et al.* [139] where a phase mask is used with a conventional optical system in order to introduce a rotating PSF with the distance. The phase mask is developed with Si nano-disk in a SiO_2 matrix and operates at 1550 nm.

Shen *et al.* [140] experimentally demonstrate a compact monocular camera equipped with a single-layer metalens (silicon rectangular nanopillars on a sapphire substrate) that can capture in a single shot a 4D image under ambient illumination conditions. The metalens produces two slightly shifted twin images with orthogonal polarizations, where each point appears as a single-helix PSF whose rotation encodes depth, while the image displacement reveals polarization information. Starting from the latter images an algorithm, based on image segmentation and calculation of the local orientation of the translation vector of the object pair, allow to reconstruct 2D all-in-focus intensity, depth, and polarization of a target scene.

Metalenses, with their ability to control light at subwavelength scales, have found innovative applications to encode advanced optical functions, including edge detection [141,142]. Edge detection is crucial for distinguishing boundaries between objects, enhancing the contrast of sharp transitions in light intensity. Edge detection is a fundamental tool in image processing, computing, and machine vision.

Metalenses can be designed to perform spatial differentiation, a key operation in edge detection, by engineering the phase profile of the metasurface. By controlling the phase shift across the lens surface, metalenses can amplify high-frequency components of an image, effectively highlighting edges. This process reduces the need for post-processing and enables real-time detection in compact optical systems. The use of metalenses for edge detection holds significant potential in fields like microscopy, object recognition, and autonomous systems, where detecting boundaries and shapes is critical. In this perspective, in 2021 Chen *et al.* [143] proposed a metalens-based light field camera (also known as plenoptic camera). A plenoptic camera is capable to capture not only the intensity distribution of the scene, but also the direction of the incoming light. The proposed implementation addresses in particular the problem of 3-D edge detection, i.e. not only the individuation of edges of the object (in the vertical and horizontal direction, i.e. 2-D) but also the determination of the distance of the edges from the camera.

The system is based on a gallium nitride achromatic metalens array. The array consists of 60 by 60 achromatic metalenses, which operate in the visible range from 400 to 660 nm. According to the plenoptic camera principle, each metalens of the array creates on the focal plane detector an image of the scene from a different staring direction and a different object plane distance. This allows all of the light field information of objects in the scene to be captured and computed. For each sub image, the edge information is digitally extracted by subtraction of the image by

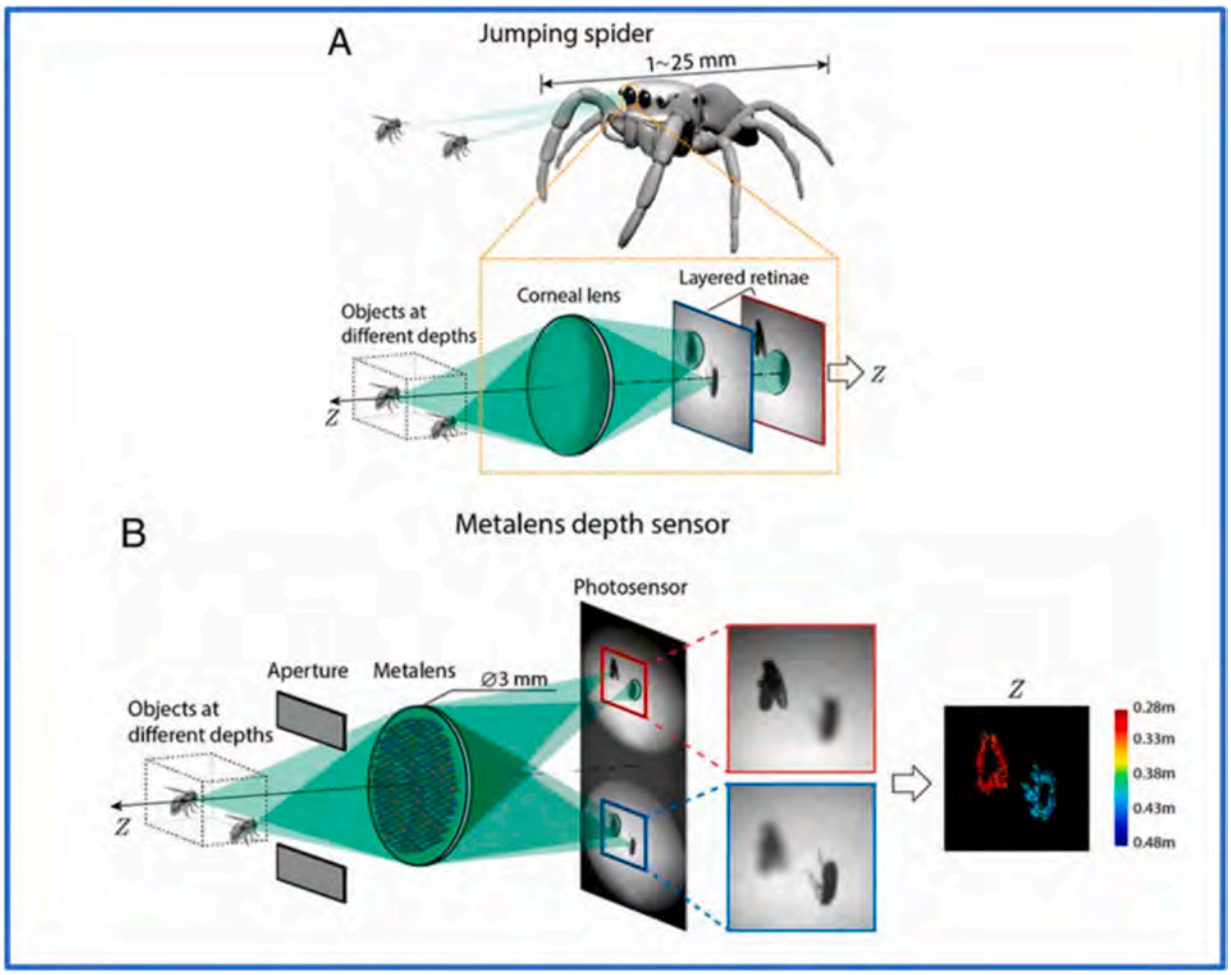

Fig. 10. Implementation and operation example of a metalens based depth sensor. **(A)** Jumping spiders can sense depth using either 1 of their 2 front-facing principal eyes, jumping spiders have multiple retinae that are layered and semi-transparent and can simultaneously measure multiple images of the same scene with different amounts of defocus. **(B)** The metalens depth sensor estimates depth by mimicking the jumping spider, capturing 2 images with different defocus, and using efficient calculations to produce depth from these images. The metalens operates at 532 nm. The depth map computed by the sensor is shown on the right, with color used to represent object distance. The closer and farther flies are colored red and blue, respectively. Readapted from reference [131] under licence CC BY-NC 4.0.

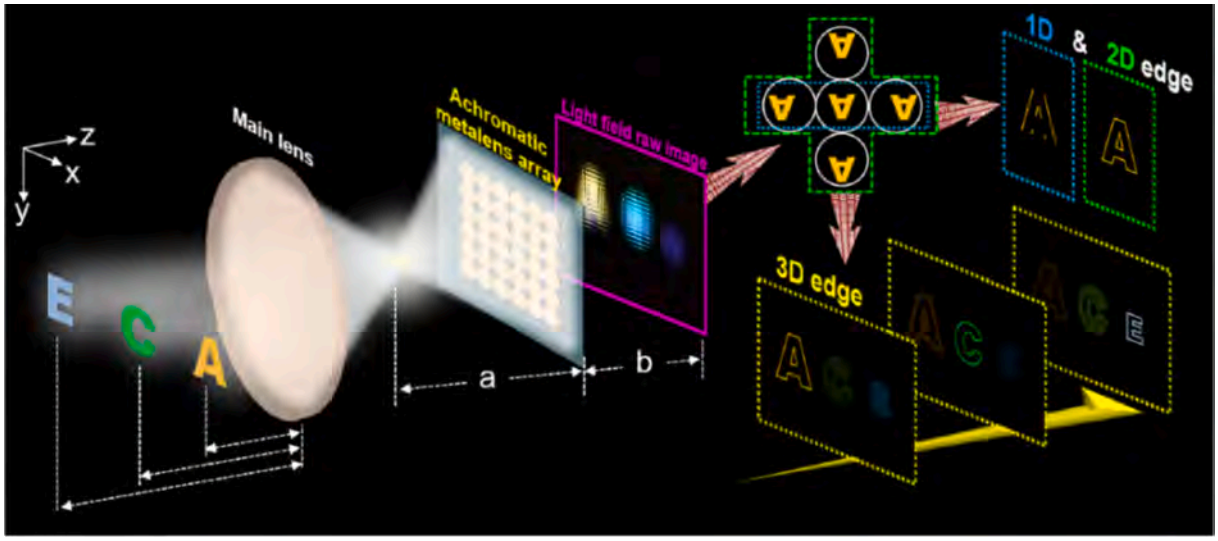

Fig. 11. Schematic diagram of multidimensional edge detection with light-field imaging (panoptic camera) system by the achromatic metalens array. Reproduced from [143] under licence CC BY-NC 4.0.

itself with a 1-pixel shift in the *x* or *y* direction. The distance estimation of the edges so found is obtained by measuring the parallax between the images from neighbouring elements of the lenslet array (with a method usually defined as disparity analysis). Therefore, as a result of the image processing not only the edges localization is obtained but also their depth estimation is provided. The operating principle of this device is shown in the Fig. 11.

This topic was also investigated in other papers, such as [144,145]. In reference [138], Wang and colleagues studied the specific mechanism of edge detection via metalenses by focusing on phase modulation techniques. The study details how metalenses are engineered to perform spatial differentiation, which is a mathematical operation that enhances the contrast between high-frequency and low-frequency spatial components of an image. Wang's team designed a metalens with nanoscale phase gradients, optimized to selectively amplify the image edges through precise control over the propagation phase of incident light waves. The research further quantifies how subwavelength structures within the metalens are tailored to operate across specific spectral bands, allowing for real-time edge detection at multiple wavelengths. The study demonstrated edge detection with a resolution down to 200 nm over the visible light spectrum, showcasing the potential for practical imaging applications. In reference [139], the approach to metalens-based edge detection is extended to broadband imaging systems. The paper explores the integration of polarization-insensitive metalenses, in hyperspectral edge detection systems. Zhou's team focused on how these lenses can perform phase gradient manipulations to extract edge features across different spectral ranges. The study highlights the use of plasmonic and dielectric metasurfaces, showing high efficiency across both visible and infrared wavelengths. This allows for simultaneous edge detection at multiple frequencies, offering advantages in multi-spectral and hyperspectral imaging setups.

In order to overcome limitations of metalenses in terms of focusing efficiency due to chromatic and angular aberration some authors have proposed the integration of DNN-based image post processing in imaging systems [146]. The imaging system addressed in [147] consists of a 10 mm diameter metalens composed of TiO_2 nanopillars on a glass wafer (realized by NIL and subsequent thin-film deposition of TiO_2) and a DNN trained for image post-processing, operating in the range visible range. By concatenating the restoration framework to the imaging system based on a mass-produced metalens, the authors obtained integrated imaging delivering high-quality images.

In recent years, the integration of computational imaging and deep learning has emerged as a powerful strategy for advancing the performance of ultra-compact optical systems. This hybrid approach leverages the complementary strengths of optics and computation, redistributing system complexity by offloading aberration correction and image enhancement tasks to learned, data-driven algorithms. In particular, convolutional neural networks (CNNs) have shown substantial promise in compensating for the image degradation introduced by simplified or miniaturized optical designs. Typical CNNs implementations involve encoder-decoder architectures or U-Nets [148,149] trained on paired datasets of degraded and ground-truth images. The training of these encoder-decoder architectures can be achieved through the optimization of merit functions such as: pixel-wise (mean square error or mean absolute error) [150], perceptual (visual geometry group-based) [151], and structural (structural similarity index, peak signal-to-noise ratio) [152,153]. These networks are often embedded in differentiable physics-based models of the optical system, allowing end-to-end joint training of both optical and computational components [154–156]. A key enabler of this paradigm shift is the development of end-to-end differentiable co-design frameworks, where both the physical characteristics of the optical system and the image reconstruction algorithm are jointly optimized as a single computational graph. Within such frameworks, models of the PSF, aperture geometry, and aberration profiles are embedded into the training loop, allowing simultaneous learning of both the optical front-end and the digital back-end. One representative example of this approach is presented in [154], where the authors propose a *meta*-imager comprising a single metalens and an aperture stop, integrated on opposite sides of a 1-mm-thick glass substrate. This physical configuration effectively mitigates off-axis aberrations such as coma and astigmatism. The optical elements are co-optimized with a CNN-based image restoration module via a fully differentiable pipeline. Experimental results demonstrate full-color imaging across the entire visible spectrum with a 70° field of view, along with reduced blur in the raw sensor data, significantly easing the computational burden during post-processing. This architecture represents a compelling advancement toward deployable nanophotonic imaging systems with commercial viability. Another work that exploits the synergy between metasurface optics and computational imaging is detailed in [156], where the authors address the long-standing challenge of chromatic aberration in diffractive optical systems. They design a metalens with a spectrally invariant PSF that maintains image focus across the visible spectrum (400–700 nm) under broadband (white-light) illumination. The spectral invariance of the PSF enables image reconstruction using a single wavelength-independent digital filter, eliminating the need for multiple correction kernels and simplifying the reconstruction pipeline. This solution offers a practical path to full-color, compact imaging systems without the need for complex multi-layer or narrowband optics. A further demonstration of joint physical-computational optimization is presented in [153], where a neural nano-optics imager is developed using a differentiable design framework that simultaneously learns the metasurface geometry and the parameters of a feature-based neural reconstruction algorithm. The resulting imager achieves a field of view significantly wider than prior full-color metasurface cameras, along with the largest demonstrated aperture (0.5 mm) at a f-number of 2. Notably, the system achieves an order-of-magnitude lower reconstruction error compared to previous compact metasurface imagers, further closing the performance gap between flat optics and conventional refractive systems. Beyond image restoration, machine learning has also been utilized to expand the functional scope of optical systems into the realm of machine vision. A particularly novel approach is described in [155], where a *meta*-imager performs optical-domain convolution operations using metasurfaces engineered for polarization and angular multiplexing. These metasurfaces encode both positive and negative convolution kernels in a single optical shot, producing multiple feature channels that are subsequently processed by a lightweight digital classifier. The system achieves classification accuracies of 98.6 % handwritten digits and 88.8 % accuracy in fashion images, with low power consumption and high throughput, highlighting its suitability for real-time inference in edge computing and embedded systems.

Despite these compelling advances, several limitations persist that must be critically addressed to enable widespread deployment of learning-based computational imagers. First, the availability and representativeness of training datasets remains a bottleneck. While synthetic datasets can be generated at scale via physics-based optical simulations, they frequently fail to capture real-world variations such as sensor noise, scene diversity, and manufacturing imperfections. This domain mismatch can lead to poor generalization during inference. It is possible to mitigate this issue by incorporating experimentally captured calibration images and applying data augmentation techniques to improve robustness. Second, noise robustness remains an open challenge. Ultra-compact optical systems often suffer from limited photon collection efficiency, resulting in low SNR, particularly under practical lighting conditions. While certain architectures incorporate pre-processing steps such as denoising filters, others rely on end-to-end training of neural networks that implicitly learn to suppress noise. Nonetheless, performance under high-noise scenarios is often suboptimal and necessitates the development of more explicit noise modelling strategies during training. Third, generalization to out-of-distribution inputs is a known limitation of deep learning-based systems. Many models exhibit strong performance on data distributions similar to their

training sets but degrade significantly when applied to novel object categories, lighting conditions, or changes in optical configurations. This sensitivity constrains the adaptability of such systems to real-world scenarios. Techniques such as domain adaptation, contrastive learning, and few-shot fine-tuning are being actively explored but remain areas of ongoing research. Finally, computational and energy efficiency are critical considerations for embedded and real-time applications. Traditional DNNs incur substantial computational and power demands. To address this, hybrid optical-electronic architectures have been proposed, where portions of the inference workload, such as convolution, are offloaded to the optical domain using programmable metasurfaces [155]. Although these designs significantly reduce digital processing requirements, they are currently limited to task-specific inference (e.g., classification) and have not yet been generalized to high-fidelity image reconstruction or multi-purpose vision tasks.

3.4. Practical challenges and future directions for Metalens-Based optical systems

Despite remarkable advances, several practical challenges must be addressed before metalenses can be translated from laboratory prototypes to widely adopted components in commercial optical platforms. A fundamental limitation is the inherent trade-off between NA, efficiency, and operational bandwidth. High-NA designs often suffer from reduced efficiency and narrowband performance, whereas achromatic operation across the visible spectrum still requires complex dispersion engineering and typically sacrifices throughput. The lack of standardized metrology further complicates benchmarking, as metrics such as focusing efficiency, Strehl ratio, and encircled energy are often reported inconsistently across publications, making direct comparison difficult.

Besides, design of metalenses is still a challenging task. As the operation of the metalens relies with the interaction of the electromagnetic wave with individual *meta*-atoms, standard optical design methods (e.g. ray tracing methods) cannot be used, and full wave simulation methods are required to properly take into account near field effects. These methods are already implemented in public domain or commercial software packages, and they are able to accurately simulate the behaviour of single *meta*-atoms or small *meta*-atoms set. Nonetheless, the full modelling and optimization of the large set of *meta*-atoms that compose a metalens (which is at least of the order of $(D/\lambda)^2$ elements where D is the diameter and λ is the working wavelength) severely challenges currently available computational capabilities, unless strong simplifications and approximations are adopted. Moreover, the results of full wave simulation methods hardly merge with currently available ray tracing optical simulation software packages, which are the *de facto* standard in optics industrial design.

Future directions in metalens research point toward multifunctional designs that simultaneously address chromatic dispersion, angular response, and polarization control, thereby overcoming the limitations of single-function devices. Equally promising is the development of active and tunable approaches, which enable dynamic reconfiguration of optical properties in real time.

One of the most pressing issue concerns the scalability of metalenses production. EBL has been the workhorse technique for prototyping metalenses, providing sub-10 nm resolution and exceptional design flexibility. Its capability to define arbitrary patterns with high fidelity has enabled many of the pioneering demonstrations in *meta*-optics. However, EBL suffers from intrinsically low throughput due to its serial writing nature, alongside high cost and field-stitching errors in large-area fabrication. These limitations make EBL ideal for research and small-scale prototyping, but unsuitable for scalable, wafer-level manufacturing required for commercial deployment.

Several scalable fabrication techniques are under exploration to enable mass production of metalenses. DUV photolithography, already employed in STMicroelectronics–Metalenz commercial modules, offers CMOS compatibility and sub-100 nm resolution on 200–300 mm wafers, though at high initial cost. NIL provides a low-cost and large-area samples alternative suitable for consumer optics, including roll-to-roll variants for flexible and wearable devices, albeit with uniformity and mould durability concerns. Other approaches such as Nanotransfer Lithography (NTL) roll-to-plate, and 3D nanoimprinting are emerging, promising rapid large-area patterning and nanometer-scale resolution [157,158].

DUV lithography and NIL are beginning to demonstrate the potential for the mass production of both cost-effective and environmentally friendly metasurfaces [159,160].

From a system-integration perspective, challenges remain in aligning and packaging metalenses with CMOS or CCD image sensors. Precise control of spacing, mitigation of stray reflections, and the implementation of broadband anti-reflective coatings are critical to ensure robust operation. Direct on-chip integration in compact packaging is required, however combining nanostructured materials with standard microelectronic fabrication processes remains highly challenging.

Recent demonstrations of on-chip achromatic metalens arrays compatible with CMOS fabrication [161] and polarization-sensitive metasurface cameras for full-Stokes imaging [133] highlight the potential of hybrid architectures combining *meta*-optics and CMOS-based imaging.

In summary, metalenses are rapidly advancing toward real-world implementations, yet their widespread adoption still hinges on solving practical challenges in efficiency, scalability, and system integration. The convergence of scalable nanofabrication methods, multifunctional designs, and hybrid computational architectures will be decisive in overcoming these barriers. With these challenges addressed, metalenses can redefine the landscape of modern optics.

4. Conclusions

Metalens technology is paving the way for significant advancements in optical systems, offering compact, lightweight alternatives to traditional lenses. In the last years, research on metalenses technology has accelerated, introducing significant innovations that are poised to reshape optical systems. Recent publications highlight key advancements in areas such as achieving higher focusing efficiencies, obtaining near diffraction limited focusing performances, broadening the spectral range, and developing metalenses that offer tunable and/or multifunctional capabilities. For instance, efforts have been made to improve chromatic aberration correction and to integrate metalenses into multispectral and hyperspectral imaging systems. Moreover, new research emphasizes the potential of metalenses for compact optical systems in fields such as augmented reality, space exploration, and telecommunications. Notably, passive distance measurement and enhanced edge detection techniques using metalenses have gained attraction, providing a new avenue for integrating deep learning to restore and enhance image quality in real-time. These developments suggest that metalenses will play a pivotal role in future high-resolution, scalable, and adaptable optical systems, pushing the boundaries of what is possible in fields requiring precision and miniaturization.

Looking forward, the integration of active metalenses, which can dynamically adjust focal lengths or other properties under external stimuli, is likely to be a major focus. This direction promises to expand the use of metalenses into new domains, from consumer electronics to highly specialized scientific research. Moreover, the integration of metasurfaces directly onto CMOS sensors will enable the development of ultrathin imaging systems with snapshot capabilities for capturing polarization, spectral, and depth information simultaneously.

Advancements in scalable fabrication techniques, such as NIL and DUV lithography, will play a significant role for the transition of metalens technology from laboratory prototypes to industrial-scale production.

CRediT authorship contribution statement

B. Patrizi: Writing – review & editing, Writing – original draft, Visualization, Validation, Data curation, Conceptualization. **A. Santonocito:** Writing – review & editing, Visualization. **G. Toci:** Writing – review & editing, Writing – original draft, Project administration, Conceptualization.

Declaration of competing interest

The authors declare that they have no known competing financial interests or personal relationships that could have appeared to influence the work reported in this paper.

Acknowledgement

This work was partially supported by the Regione Toscana through the European Social Fund Plus, regional program 2021–2027, Project METALENS.

Data availability

No data was used for the research described in the article.

References

[1] Y. He, B. Song, J. Tang, Optical metalenses: fundamentals, dispersion manipulation, and applications, Front. Optoelectron. 15 (1) (2022) 24.
[2] S. Jahani, Z. Jacob, All-dielectric metamaterials, Nat Nanotechnol [Internet]. 11 (1) (2016) 23–36, https://doi.org/10.1038/nnano.2015.304.
[3] M. Schake, Examining and explaining the "generalized laws of reflection and refraction" at metasurface gratings, Available from, J Opt Soc Am A [internet]. 39 (8) (2022) 1352–1359, https://opg.optica.org/josaa/abstract.cfm?URI=josaa-39-8-1352.
[4] N. Yu, P. Genevet, M.A. Kats, F. Aieta, J.P. Tetienne, F. Capasso, et al., Light propagation with phase discontinuities: Generalized laws of reflection and refraction, Science (80-) [Internet]. 334 (6054) (2011 Oct) 333–337, https://doi.org/10.1126/science.1210713.
[5] M. Decker, I. Staude, M. Falkner, J. Dominguez, D.N. Neshev, I. Brener, et al., High-Efficiency Dielectric Huygens' Surfaces, Adv. Opt. Mater. 3 (6) (2015 Jun) 813–820.
[6] S. Zhang, H. Zhou, B. Liu, Z. Su, L. Huang, Recent advances and prospects of Optical Metasurfaces, ACS Photonics 10 (7) (2023 Jul) 2045–2063.
[7] A. Santonocito, B. Patrizi, G. Toci, Recent advances in Tunable Metasurfaces and their Application in Optics, Nanomaterials 13 (10) (2023).
[8] S. Roy, K. Debnath, Electromechanically tunable graphene-based terahertz metasurface, Opt. Commun. 534 (2023) 129319.
[9] X. Ou, T. Zeng, Y. Zhang, Y. Jiang, Z. Gong, F. Fan, et al., Tunable Polarization-Multiplexed Achromatic Dielectric Metalens, Nano Lett. 22 (24) (2022 Dec) 10049–10056.
[10] C. Zheng, J. Li, L. Liu, J. Li, Z. Yue, X. Hao, et al., Optically Tunable Terahertz Metasurface Absorber, Ann. Phys. 534 (5) (2022 May) 2200007.
[11] A. Arbabi, A. Faraon, Advances in optical metalenses, Nat. Photonics 17 (1) (2023) 16–25.
[12] Y. Li, X. Huang, S. Liu, H. Liang, Y. Ling, Y. Su, Metasurfaces for near-eye display applications, Opto-Electronic Sci. 2 (8) (2023) 230021–230025.
[13] W.T. Chen, A.Y. Zhu, V. Sanjeev, M. Khorasaninejad, Z. Shi, E. Lee, et al., A broadband achromatic metalens for focusing and imaging in the visible, Nat. Nanotechnol. 13 (3) (2018) 220–226.
[14] M. Khorasaninejad, W.T. Chen, R.C. Devlin, J. Oh, A.Y. Zhu, F. Capasso, Metalenses at visible wavelengths: Diffraction-limited focusing and subwavelength resolution imaging, Science (80-) [Internet]. 352 (6290) (2016 Jun) 1190–1194, https://doi.org/10.1126/science.aaf6644.
[15] S.W. Moon, Y. Kim, G. Yoon, J. Rho, Recent Progress on Ultrathin Metalenses for Flat Optics, iScience 23 (12) (2020) 101877.
[16] M. Pan, Y. Fu, M. Zheng, H. Chen, Y. Zang, H. Duan, et al., Dielectric metalens for miniaturized imaging systems: progress and challenges, Light Sci Appl [Internet]. 11 (1) (2022) 195, https://doi.org/10.1038/s41377-022-00885-7.
[17] A. Alù, N. Engheta, Input Impedance, Nanocircuit Loading, and Radiation Tuning of Optical Nanoantennas, Phys. Rev. Lett. 101 (4) (2008 Jul) 43901.
[18] P. Biagioni, M. Savoini, J.S. Huang, L. Duò, M. Finazzi, B. Hecht, Near-field polarization shaping by a near-resonant plasmonic cross antenna, Phys. Rev. B 80 (15) (2009 Oct) 153409.
[19] T. Sun, J. Hu, S. Ma, F. Xu, C. Wang, Polarization-insensitive achromatic metalens based on computational wavefront coding, Opt. Express 29 (20) (2021) 31902–31914.
[20] F. Ding, Y. Yang, R.A. Deshpande, S.I. Bozhevolnyi, A Review of Gap-Surface Plasmon Metasurfaces: Fundamentals and Applications. 7 (6) (2018) 1129–1156.
[21] B.H. Chen, P.C. Wu, V.C. Su, Y.C. Lai, C.H. Chu, I.C. Lee, et al., GaN Metalens for Pixel-Level Full-Color Routing at Visible Light, Nano Lett. 17 (10) (2017 Oct) 6345–6352.
[22] P. Genevet, F. Capasso, F. Aieta, M. Khorasaninejad, R. Devlin, Recent advances in planar optics: from plasmonic to dielectric metasurfaces, Optica 4 (1) (2017) 139–152.
[23] L. Li, J. Zhang, Y. Hu, J. Lai, S. Wang, P. Yang, et al., Broadband Polarization-Switchable Multi-Focal Noninterleaved Metalenses in the Visible, Laser Photon Rev. 15 (11) (2021 Nov) 2100198.
[24] P.S. Huang, C.H. Chu, S.H. Huang, H.P. Su, T. Tanaka, P.C. Wu, Varifocal Metalenses: Harnessing Polarization-Dependent Superposition for Continuous Focal Length Control, Nano Lett. 23 (22) (2023 Nov) 10432–10440.
[25] Q. Fan, Y. Wang, M. Liu, T. Xu, High-efficiency, linear-polarization-multiplexing metalens for long-wavelength infrared light, Opt. Lett. 43 (24) (2018) 6005–6008.
[26] R.C. Jones, A New Calculus for the Treatment of Optical SystemsI. Description and Discussion of the Calculus, Available from: J Opt Soc Am [internet]. 31 (7) (1941) 488–493 https://opg.optica.org/abstract.cfm?URI=josa-31-7-488.
[27] A. Kalvach, Z. Szabó, Aberration-free flat lens design for a wide range of incident angles, J. Opt. Soc. Am. B 33 (2) (2016) A66–A71.
[28] J.P. Balthasar Mueller, N.A. Rubin, R.C. Devlin, B. Groever, F. Capasso, Metasurface polarization optics: independent phase control of arbitrary orthogonal states of polarization, Phys. Rev. Lett. 118 (11) (2017) 113901.
[29] S. Li, X. Li, G. Wang, S. Liu, L. Zhang, C. Zeng, et al., Multidimensional manipulation of photonic spin Hall effect with a single-layer dielectric metasurface, Adv. Opt. Mater. 7 (5) (2019) 1801365.
[30] M. Khorasaninejad, W.T. Chen, A.Y. Zhu, J. Oh, R.C. Devlin, C. Roques-Carmes, et al., Visible Wavelength Planar Metalenses based on Titanium Dioxide, IEEE J. Sel. Top. Quantum Electron. 23 (3) (2017) 43–58.
[31] C. Chen, S. Gao, W. Song, H. Li, S.N. Zhu, T. Li, Metasurfaces with planar chiral meta-atoms for spin light manipulation, Nano Lett. 21 (4) (2021) 1815–1821.
[32] A.L. Holsteen, D. Lin, I. Kauvar, G. Wetzstein, M.L. Brongersma, A Light-Field Metasurface for High-Resolution Single-Particle Tracking, Nano Lett. 19 (4) (2019 Apr) 2267–2271.
[33] M. Faraji-Dana, E. Arbabi, A. Arbabi, S.M. Kamali, H. Kwon, A. Faraon, Compact Folded Metasurface Spectrometer. Nat Commun. 9 (1) (2018) 4196.
[34] R.J. Lin, V.C. Su, S. Wang, M.K. Chen, T.L. Chung, Y.H. Chen, et al., Achromatic metalens array for full-colour light-field imaging, Nat. Nanotechnol. 14 (3) (2019) 227–231.
[35] H. Pahlevaninezhad, M. Khorasaninejad, Y.W. Huang, Z. Shi, L.P. Hariri, D. C. Adams, et al., Nano-optic endoscope for high-resolution optical coherence tomography in vivo, Nat. Photonics 12 (9) (2018) 540–547.
[36] E. Arbabi, S.M. Kamali, A. Arbabi, A. Faraon, Full-Stokes Imaging Polarimetry using Dielectric Metasurfaces, ACS Photonics 5 (8) (2018 Aug) 3132–3140.
[37] C. Schlickriede, N. Waterman, B. Reineke, P. Georgi, G. Li, S. Zhang, et al., Imaging through Nonlinear Metalens using Second Harmonic Generation, Adv. Mater. 30 (8) (2018 Feb) 1703843.
[38] C. Schlickriede, S.S. Kruk, L. Wang, B. Sain, Y. Kivshar, T. Zentgraf, Nonlinear Imaging with All-Dielectric Metasurfaces, Nano Lett. 20 (6) (2020) 4370–4376.
[39] A. Small, Spherical aberration, coma, and the Abbe sine condition for physicists who don't design lenses, Am. J. Phys 86 (7) (2018 Jul) 487–494.
[40] M.J. Riedl, Optical Design Fundamentals for Infrared Systems, Society of Photo Optical (2001). SPIE tutorial texts.
[41] L.C.R. Jr, M.D. Perrin, F. Marchis, A. Sivaramakrishnan, R.B. Makidon, J. C. Christou, et al., Is that really your Strehl ratio? In: Procspie. (2004) 504–515.
[42] J. Engelberg, C. Zhou, N. Mazurski, J. Bar-David, A. Kristensen, U. Levy, Near-IR Wide-Field-of-View Huygens Metalens for Outdoor Imaging Applications. 9 (2) (2020) 361–370.
[43] M.Y. Shalaginov, S. An, F. Yang, P. Su, D. Lyzwa, A.M. Agarwal, et al., Single-Element Diffraction-Limited Fisheye Metalens, Nano Lett. 20 (10) (2020 Oct) 7429–7437.
[44] A. Arbabi, E. Arbabi, S.M. Kamali, Y. Horie, S. Han, A. Faraon, Miniature optical planar camera based on a wide-angle metasurface doublet corrected for monochromatic aberrations, Nat. Commun. 7 (1) (2016) 13682.
[45] B. Groever, W.T. Chen, F. Capasso, Meta-Lens Doublet in the Visible Region, Nano Lett. 17 (8) (2017 Aug) 4902–4907.
[46] M. Jang, Y. Horie, A. Shibukawa, J. Brake, Y. Liu, S.M. Kamali, et al., Wavefront shaping with disorder-engineered metasurfaces, Nat. Photonics 12 (2) (2018) 84–90.
[47] J. Xu, M. Cua, E.H. Zhou, Y. Horie, A. Faraon, C. Yang, Wide-angular-range and high-resolution beam steering by a metasurface-coupled phased array, Opt. Lett. 43 (21) (2018) 5255–5258.
[48] T. Xie, F. Zhang, M. Pu, H. Bao, J. Jin, J. Cai, et al., Ultrathin, Wide-Angle, and High-Resolution Meta-Imaging System via Rear-Position Wavevector Filter, Laser Photon Rev. 17 (9) (2023 Sep) 2300119.
[49] A. Martins, K. Li, J. Li, H. Liang, D. Conteduca, B.H.V. Borges, et al., On Metalenses with Arbitrarily Wide Field of View, ACS Photonics 7 (8) (2020 Aug) 2073–2079.
[50] M. Pu, X. Li, Y. Guo, X. Ma, X. Luo, Nanoapertures with ordered rotations: symmetry transformation and wide-angle flat lensing, Opt. Express 25 (25) (2017) 31471–31477.
[51] F. Zhang, M. Pu, X. Li, X. Ma, Y. Guo, P. Gao, et al., Extreme-Angle Silicon Infrared Optics Enabled by Streamlined Surfaces, Adv. Mater. 33 (11) (2021 Mar) 2008157.

[52] A. Wirth-Singh, J.E. Fröch, Z. Han, L. Huang, S. Mukherjee, Z. Zhou, et al., Large field-of-view thermal imaging via all-silicon meta-optics, Appl. Opt. 62 (20) (2023) 5467–5474.

[53] H.I. Lin, J. Geldmeier, E. Baleine, F. Yang, S. An, Y. Pan, et al., Wide-Field-of-View, Large-Area Long-Wave Infrared Silicon Metalenses, ACS Photonics 11 (5) (2024 May) 1943–1949.

[54] O. Kigner, M. Meem, B. Baker, S. Banerji, P.W.C. Hon, B. Sensale-Rodriguez, et al., Monolithic all-silicon flat lens for broadband LWIR imaging, Opt. Lett. 46 (16) (2021) 4069–4071.

[55] J.S. Park, S.W.D. Lim, A. Amirzhan, H. Kang, K. Karrfalt, D. Kim, et al., All-Glass 100 mm Diameter Visible Metalens for Imaging the Cosmos, ACS Nano 18 (4) (2024 Jan) 3187–3198.

[56] W.T. Chen, A.Y. Zhu, M. Khorasaninejad, Z. Shi, V. Sanjeev, F. Capasso, Immersion Meta-Lenses at Visible Wavelengths for Nanoscale Imaging, Nano Lett. 17 (5) (2017 May) 3188–3194.

[57] R. Paniagua-Domínguez, Y.F. Yu, E. Khaidarov, S. Choi, V. Leong, R.M. Bakker, et al., A Metalens with a Near-Unity Numerical Aperture, Nano Lett. 18 (3) (2018 Mar) 2124–2132.

[58] D. Lin, P. Fan, E. Hasman, M.L. Brongersma, Dielectric gradient metasurface optical elements, Science (80-) 345 (6194) (2014 Jul) 298–302.

[59] A. Arbabi, R.M. Briggs, Y. Horie, M. Bagheri, A. Faraon, Efficient dielectric metasurface collimating lenses for mid-infrared quantum cascade lasers, Opt. Express 23 (26) (2015) 33310–33317.

[60] H. Liang, Q. Lin, X. Xie, Q. Sun, Y. Wang, L. Zhou, et al., Ultrahigh Numerical Aperture Metalens at Visible Wavelengths, Nano Lett. 18 (7) (2018 Jul) 4460–4466.

[61] Q. Fan, M. Liu, C. Yang, L. Yu, F. Yan, T. Xu, A high numerical aperture, polarization-insensitive metalens for long-wavelength infrared imaging, Appl. Phys. Lett. 113 (20) (2018 Nov) 201104.

[62] M. Born, E. Wolf, Principles of Optics: Electromagnetic Theory of Propagation, Elsevier Science, Interference and Diffraction of Light, 2013.

[63] S. Wang, P.C. Wu, V.C. Su, Y.C. Lai, C. Hung Chu, J.W. Chen, et al., Broadband achromatic optical metasurface devices, Nat Commun [Internet]. 8 (1) (2017) 187, https://doi.org/10.1038/s41467-017-00166-7.

[64] F. Presutti, F. Monticone, Focusing on bandwidth: achromatic metalens limits, Optica 7 (6) (2020) 624–631.

[65] Y. Zhou, I.I. Kravchenko, H. Wang, J.R. Nolen, G. Gu, J. Valentine, Multilayer Noninteracting Dielectric Metasurfaces for Multiwavelength Metaoptics, Nano Lett. 18 (12) (2018 Dec) 7529–7537.

[66] H.H. Hsiao, Y.H. Chen, R.J. Lin, P.C. Wu, S. Wang, B.H. Chen, et al., Integrated Resonant Unit of Metasurfaces for Broadband Efficiency and phase Manipulation, Adv. Opt. Mater. 6 (12) (2018 Jun) 1800031.

[67] S. Shrestha, A.C. Overvig, M. Lu, A. Stein, N. Yu, Broadband achromatic dielectric metalenses, Light Sci Appl [Internet]. 7 (1) (2018) 85, https://doi.org/10.1038/s41377-018-0078-x.

[68] K. Dou, X. Xie, M. Pu, X. Li, X. Ma, C. Wang, et al., Off-axis multi-wavelength dispersion controlling metalens for multi-color imaging, Opto-Electronic Adv. 3 (4) (2020) 190001–190005.

[69] Z. Lin, B. Groever, F. Capasso, A.W. Rodriguez, M. Lončar, Topology-Optimized Multilayered Metaoptics. Phys Rev Appl. 9 (4) (2018 Apr) 44030.

[70] W.T. Chen, A.Y. Zhu, J. Sisler, Z. Bharwani, F. Capasso, A broadband achromatic polarization-insensitive metalens consisting of anisotropic nanostructures, Nat. Commun. 10 (1) (2019) 355.

[71] D. Lin, A.L. Holsteen, E. Maguid, G. Wetzstein, P.G. Kik, E. Hasman, et al., Photonic Multitasking Interleaved Si Nanoantenna Phased Array, Nano Lett. 16 (12) (2016 Dec) 7671–7676.

[72] K. Li, Y. Guo, M. Pu, X. Li, X. Ma, Z. Zhao, et al., Dispersion controlling meta-lens at visible frequency, Opt. Express 25 (18) (2017) 21419–21427.

[73] E. Arbabi, A. Arbabi, S.M. Kamali, Y. Horie, A. Faraon, Multiwavelength metasurfaces through spatial multiplexing, Sci. Rep. 6 (1) (2016) 32803.

[74] Li Z, Lin P, Huang YW, Park JS, Chen WT, Shi Z, et al. Meta-optics achieves RGB-achromatic focusing for virtual reality. Sci Adv. 2025 Sep; 7(5):eabe4458.

[75] A. McClung, M. Mansouree, A. Arbabi, At-will chromatic dispersion by prescribing light trajectories with cascaded metasurfaces, Light Sci. Appl. 9 (1) (2020) 93.

[76] J. Hu, C.H. Liu, X. Ren, L.J. Lauhon, T.W. Odom, Plasmonic Lattice Lenses for Multiwavelength Achromatic focusing, ACS Nano 10 (11) (2016 Nov) 10275–10282.

[77] F. Aieta, M.A. Kats, P. Genevet, F. Capasso, Multiwavelength achromatic metasurfaces by dispersive phase compensation, Science (80-) 347 (6228) (2015 Mar) 1342–1345.

[78] E. Arbabi, A. Arbabi, S.M. Kamali, Y. Horie, A. Faraon, Controlling the sign of chromatic dispersion in diffractive optics with dielectric metasurfaces, Optica 4 (6) (2017) 625–632.

[79] S. Wang, P.C. Wu, V.C. Su, Y.C. Lai, M.K. Chen, H.Y. Kuo, et al., A broadband achromatic metalens in the visible, Nat. Nanotechnol. 13 (3) (2018) 227–232.

[80] M. Li, S. Li, L.K. Chin, Y. Yu, D.P. Tsai, R. Chen, Dual-layer achromatic metalens design with an effective Abbe number, Opt. Express 28 (18) (2020) 26041–26055.

[81] W. Feng, J. Zhang, Q. Wu, A. Martins, Q. Sun, Z. Liu, et al., RGB Achromatic Metalens Doublet for Digital Imaging, Nano Lett. 22 (10) (2022 May) 3969–3975.

[82] C. Kim, S.J. Kim, B. Lee, Doublet metalens design for high numerical aperture and simultaneous correction of chromatic and monochromatic aberrations, Opt. Express 28 (12) (2020) 18059–18076.

[83] O. Avayu, E. Almeida, Y. Prior, T. Ellenbogen, Composite functional metasurfaces for multispectral achromatic optics, Nat. Commun. 8 (1) (2017) 14992.

[84] A.A. Fathnan, D.A. Powell, Bandwidth and size limits of achromatic printed-circuit metasurfaces, Available from, Opt Express [internet]. 26 (22) (2018) 29440–29450, https://opg.optica.org/oe/abstract.cfm?URI=oe-26-22-29440.

[85] J. Engelberg, U. Levy, Achromatic flat lens performance limits, Optica 8 (6) (2021) 834–845.

[86] Y. Zhu, S. Liu, Y. Chang, Y. Wang, S. Zhou, C. Wu, et al., Broadband polarization-insensitive metalens with excellent achromaticity and high efficiency for the entire visible spectrum, Appl. Phys. Lett. 122 (20) (2023 May) 201702.

[87] X. Xiao, Y. Zhao, X. Ye, C. Chen, X. Lu, Y. Rong, et al., Large-scale achromatic flat lens by light frequency-domain coherence optimization, Light Sci. Appl. 11 (1) (2022) 323.

[88] M. Meem, A. Majumder, R. Menon, Full-color video and still imaging using two flat lenses, Opt. Express 26 (21) (2018) 26866–26871.

[89] N. Mohammad, M. Meem, B. Shen, P. Wang, R. Menon, Broadband imaging with one planar diffractive lens, Sci. Rep. 8 (1) (2018) 2799.

[90] Meem M, Banerji S, Majumder A, Pies C, Oberbiermann T, Sensale-Rodriguez B, et al. Inverse-designed achromatic flat lens enabling imaging across the visible and near-infrared with diameter $>$ 3 mm and NA = 0.3. Appl Phys Lett. 2020 Jul; 117(4):41101.

[91] M. Khorasaninejad, Z. Shi, A.Y. Zhu, W.T. Chen, V. Sanjeev, A. Zaidi, et al., Achromatic Metalens over 60 nm Bandwidth in the Visible and Metalens with reverse Chromatic Dispersion, Nano Lett. 17 (3) (2017 Mar) 1819–1824.

[92] Y. Wang, Q. Chen, W. Yang, Z. Ji, L. Jin, X. Ma, et al., High-efficiency broadband achromatic metalens for near-IR biological imaging window, Nat. Commun. 12 (1) (2021) 5560.

[93] A. Ndao, L. Hsu, J. Ha, J.H. Park, C. Chang-Hasnain, B. Kanté, Octave bandwidth photonic fishnet-achromatic-metalens, Nat. Commun. 11 (1) (2020) 3205.

[94] F. Balli, M. Sultan, S.K. Lami, J.T. Hastings, A Hybrid Achromatic Metalens. Nat Commun. 11 (1) (2020) 3892.

[95] L. Zhang, J. Ding, H. Zheng, S. An, H. Lin, B. Zheng, et al., Ultra-thin high-efficiency mid-infrared transmissive Huygens meta-optics, Nat. Commun. 9 (1) (2018) 1481.

[96] Y. Wei, Y. Wang, X. Feng, S. Xiao, Z. Wang, T. Hu, et al., Compact Optical Polarization-Insensitive Zoom Metalens Doublet, Adv. Opt. Mater. 8 (13) (2020 Jul) 2000142.

[97] S. Colburn, A. Zhan, A. Majumdar, Varifocal zoom imaging with large area focal length adjustable metalenses, Optica 5 (7) (2018) 825–831.

[98] I.M. Barton, S.N. Dixit, L.J. Summers, C.A. Thompson, K. Avicola, J. Wilhelmsen, Diffractive Alvarez lens, Opt. Lett. 25 (1) (2000) 1–3.

[99] V. Saragadam, Z. Han, V. Boominathan, L. Huang, S. Tan, J.E. Fröch, et al., Foveated thermal computational imaging prototype using all-silicon meta-optics, Optica 11 (1) (2024) 18–25.

[100] S.M. Kamali, E. Arbabi, A. Arbabi, Y. Horie, A. Faraon, Highly tunable elastic dielectric metasurface lenses, Laser Photon Rev. 10 (6) (2016 Nov) 1002–1008.

[101] S. Wei, G. Cao, H. Lin, X. Yuan, M. Somekh, B. Jia, A Varifocal Graphene Metalens for Broadband Zoom Imaging Covering the Entire Visible Region, ACS Nano 15 (3) (2021 Mar) 4769–4776.

[102] F. Yang, H.I. Lin, M.Y. Shalaginov, K. Stoll, S. An, C. Rivero-Baleine, et al., Reconfigurable Parfocal Zoom Metalens, Adv. Opt. Mater. 10 (17) (2022 Sep) 2200721.

[103] M. Wang, J.S. Lee, S. Aggarwal, N. Farmakidis, Y. He, T. Cheng, et al., Varifocal Metalens using Tunable and Ultralow-loss Dielectrics, Adv. Sci. 10 (6) (2023 Feb) 2204899.

[104] S. Yu, M. Xu, M. Pu, X. Tang, Y. Zheng, Y. Guo, et al., Dynamic Nonlocal Metasurface for Multifunctional Integration via Phase-Change Materials. 13 (23) (2024) 4317–4325.

[105] T. Badloe, I. Kim, Y. Kim, J. Kim, J. Rho, Electrically Tunable Bifocal Metalens with Diffraction-Limited focusing and Imaging at Visible Wavelengths, Adv. Sci. 8 (21) (2021 Nov) 2102646.

[106] She A, Zhang S, Shian S, Clarke DR, Capasso F. Adaptive metalenses with simultaneous electrical control of focal length, astigmatism, and shift. Sci Adv. 2025 Sep; 4(2):eaap9957.

[107] M. Bosch, M. Shcherbakov, K. Won, H.S. Lee, Y. Kim, G. Shvets, Voltage-Tunable Multifunctional Zoom Imaging Metalenses, ACS Photonics 12 (2) (2025 Feb) 728–736.

[108] Y. Tao, A. Eichler, T. Holzherr, C.L. Degen, Ultrasensitive mechanical detection of magnetic moment using a commercial disk drive write head, Nat. Commun. 7 (1) (2016) 12714.

[109] D.G. Manolakis, R.B. Lockwood, T.W. Cooley, Hyperspectral imaging remote sensing: physics, sensors, and algorithms, Cambridge University Press, 2016.

[110] S.E. Qian, Hyperspectral Satellites, Evolution, and Development history, IEEE J. Sel. Top. Appl. Earth Obs. Remote Sens. 14 (2021) 7032–7056.

[111] Y.W. Wang, N.P. Reder, S. Kang, A.K. Glaser, J.T.C. Liu, Multiplexed Optical Imaging of Tumor-Directed Nanoparticles: a Review of Imaging Systems and Approaches, Nanotheranostics 1 (4) (2017) 369–388.

[112] G. Roberts, C. Ballew, T. Zheng, J.C. Garcia, S. Camayd-Muñoz, P.W.C. Hon, et al., 3D-patterned inverse-designed mid-infrared metaoptics, Nat. Commun. 14 (1) (2023) 2768.

[113] X. Zou, Y. Zhang, R. Lin, G. Gong, S. Wang, S. Zhu, et al., Pixel-level Bayer-type colour router based on metasurfaces, Nat. Commun. 13 (1) (2022) 3288.

[114] M. Miyata, N. Nemoto, K. Shikama, F. Kobayashi, T. Hashimoto, Full-color-sorting metalenses for high-sensitivity image sensors, Optica 8 (12) (2021) 1596–1604.

[115] Lapray PJ, Wang X, Thomas JB, Gouton P. Multispectral Filter Arrays: Recent Advances and Practical Implementation. Vol. 14, Sensors. 2014. p. 21626–59.

[116] C. Kim, J. Hong, J. Jang, G.Y. Lee, Y. Kim, Y. Jeong, et al., Freeform metasurface color router for deep submicron pixel image sensors, Sci. Adv. 10 (22) (2025 Sep) eadn9000.
[117] M. Faraji-Dana, E. Arbabi, H. Kwon, S.M. Kamali, A. Arbabi, J.G. Bartholomew, et al., Hyperspectral Imager with Folded Metasurface Optics, ACS Photonics 6 (8) (2019 Aug) 2161–2167.
[118] C.H. Lin, S.H. Huang, T.H. Lin, P.C. Wu, Metasurface-empowered snapshot hyperspectral imaging with convex/deep (CODE) small-data learning theory, Nat. Commun. 14 (1) (2023) 6979.
[119] J.S. Tyo, M.P. Rowe, E.N. Pugh, N. Engheta, Target detection in optically scattering media by polarization-difference imaging, Appl. Opt. 35 (11) (1996) 1855–1870.
[120] D.A. Garren, A.C. Odom, M.K. Osborn, J.S. Goldstein, S.U. Pillai, J.R. Guerci, Full-polarization matched-illumination for target detection and identification, IEEE Trans. Aerosp. Electron. Syst. 38 (3) (2002) 824–837.
[121] S.G. Demos, H.B. Radousky, R.R. Alfano, Deep subsurface imaging in tissues using spectral and polarization filtering, Opt. Express 7 (1) (2000) 23–28.
[122] C. He, H. He, J. Chang, B. Chen, H. Ma, M.J. Booth, Polarisation optics for biomedical and clinical applications: a review, Light Sci. Appl. 10 (1) (2021) 194.
[123] J.S. Tyo, D.L. Goldstein, D.B. Chenault, J.A. Shaw, Review of passive imaging polarimetry for remote sensing applications, Appl. Opt. 45 (22) (2006) 5453–5469.
[124] J. Duan, Q. Fu, C. Mo, Y. Zhu, D. Liu, Review of polarization imaging for international military application, In: Procspie. (2013) 890813.
[125] J.R. Kuhn, D. Potter, B. Parise, Imaging Polarimetric Observations of a New Circumstellar disk System, Astrophys J 553 (2) (2001) L189.
[126] J.L. Pezzaniti, D.B. Chenault, A division of aperture MWIR imaging polarimeter, In: Procspie. (2005) 58880V.
[127] P.G. Klemens, Thermal conductivity and lattice vibrational modes, In: Solid State Physics. Elsevier (1958) 1–98.
[128] X. Tu, O.J. Spires, X. Tian, N. Brock, R. Liang, S. Pau, Division of amplitude RGB full-Stokes camera using micro-polarizer arrays: erratum, Opt. Express 26 (4) (2018) 4192–4193.
[129] Q. Fan, W. Xu, X. Hu, W. Zhu, T. Yue, F. Yan, et al., Disordered metasurface enabled single-shot full-Stokes polarization imaging leveraging weak dichroism, Nat. Commun. 14 (1) (2023) 7180.
[130] Rubin NA, D'Aversa G, Chevalier P, Shi Z, Chen WT, Capasso F. Matrix Fourier optics enables a compact full-Stokes polarization camera. Science (80-). 2019 Jul; 365(6448):eaax1839.
[131] Z. Huang, Y. Zheng, J. Li, Y. Cheng, J. Wang, Z.K. Zhou, et al., High-resolution metalens imaging polarimetry, Nano Lett. 23 (23) (2023) 10991–10997.
[132] Ou K, Yu F, Li G, Wang W, Miroshnichenko AE, Huang L, et al. Mid-infrared polarization-controlled broadband achromatic metadevice. Sci Adv. 2024 Sep;6 (37):eabc0711.
[133] J. Zuo, J. Bai, S. Choi, A. Basiri, X. Chen, C. Wang, et al., Chip-integrated metasurface full-Stokes polarimetric imaging sensor, Light Sci. Appl. 12 (1) (2023) 218.
[134] Q. Zhang, P. Lin, C. Wang, Y. Zhang, Z. Yu, X. Liu, et al., Neural-Optic Co-Designed Polarization-Multiplexed Metalens for Compact Computational Spectral Imaging, Laser Photon Rev. 18 (8) (2024 Aug) 2400187.
[135] B. Fu, X. Zhou, T. Li, H. Zhu, Z. Liu, S. Zheng, et al., Miniaturized high-efficiency snapshot polarimetric stereoscopic imaging, Optica 12 (3) (2025) 391–398.
[136] S. Tan, F. Yang, V. Boominathan, A. Veeraraghavan, G.V. Naik, 3D Imaging using Extreme Dispersion in Optical Metasurfaces, ACS Photonics 8 (5) (2021 May) 1421–1429.
[137] Z.B. Fan, H.Y. Qiu, H.L. Zhang, X.N. Pang, L.D. Zhou, L. Liu, et al., A broadband achromatic metalens array for integral imaging in the visible, Light Sci. Appl. 8 (1) (2019) 67.
[138] Q. Guo, Z. Shi, Y.W. Huang, E. Alexander, C.W. Qiu, F. Capasso, et al., Compact single-shot metalens depth sensors inspired by eyes of jumping spiders, Proc. Natl. Acad. Sci. 116 (46) (2019 Nov) 22959–22965.
[139] C. Jin, M. Afsharnia, R. Berlich, S. Fasold, C. Zou, D. Arslan, et al., Dielectric metasurfaces for distance measurements and three-dimensional imaging, Adv Photonics. 1 (3) (2019 Jun) 36001.
[140] Z. Shen, F. Zhao, C. Jin, S. Wang, L. Cao, Y. Yang, Monocular metasurface camera for passive single-shot 4D imaging, Nat. Commun. 14 (1) (2023) 1035.
[141] Y. Kim, G.Y. Lee, J. Sung, J. Jang, B. Lee, Spiral Metalens for phase Contrast Imaging, Adv. Funct. Mater. 32 (5) (2022 Jan) 2106050.
[142] J. Zhou, H. Qian, C.F. Chen, J. Zhao, G. Li, Q. Wu, et al., Optical edge detection based on high-efficiency dielectric metasurface, Proc. Natl. Acad. Sci. 116 (23) (2019 Jun) 11137–11140.
[143] M.K. Chen, Y. Yan, X. Liu, Y. Wu, J. Zhang, J. Yuan, et al., Edge Detection with Meta-Lens: from One Dimension to Three Dimensions. 10 (14) (2021) 3709–3715.
[144] S. Wang, L. Li, S. Wen, R. Liang, Y. Liu, F. Zhao, et al., Metalens for Accelerated Optoelectronic Edge Detection under Ambient Illumination, Nano Lett. 24 (1) (2024 Jan) 356–361.
[145] J. Zhou, J. Zhao, Q. Wu, C.F. Chen, M. Lei, G. Chen, et al., Nonlinear Computational Edge Detection Metalens, Adv. Funct. Mater. 32 (34) (2022 Aug) 2204734.
[146] J. Seo, J. Jo, J. Kim, J. Kang, C. Kang, S. Moon, Eunji Lee, Junsuk Rho HC. Deep-learning-driven end-to-end metalens imaging. Opt Open, Jehyeong Hong, 2023.
[147] J. Kim, J. Seong, W. Kim, G.Y. Lee, S. Kim, H. Kim, et al., Scalable manufacturing of high-index atomic layer–polymer hybrid metasurfaces for metaphotonics in the visible, Nat. Mater. 22 (4) (2023) 474–481.
[148] O. Ronneberger, P. Fischer, T. Brox, in: U-Net: Convolutional Networks for Biomedical Image Segmentation BT - Medical Image Computing and Computer-Assisted Intervention – MICCAI 2015, Springer International Publishing, Cham, 2015, pp. 234–241.
[149] Zamir SW, Arora A, Khan S, Hayat M, Khan FS, Yang MH, et al. Learning Enriched Features for Real Image Restoration and Enhancement BT - Computer Vision – ECCV 2020. In: Vedaldi A, Bischof H, Brox T, Frahm JM, editors. Cham: Springer International Publishing; 2020. p. 492–511.
[150] W.L. Hsu, C.F. Huang, C.C. Tan, N.Y.C. Liu, C.H. Chu, P.S. Huang, et al., High-Resolution Metalens Imaging with Sequential Artificial Intelligence Models, Nano Lett. 23 (24) (2023 Dec) 11614–11620.
[151] R. Zhang, P. Isola, A.A. Efros, E. Shechtman, O. Wang, The Unreasonable Effectiveness of Deep Features as a Perceptual Metric, in: In: 2018 IEEE/CVF Conference on Computer Vision and Pattern Recognition (CVPR), 2018, pp. 586–595.
[152] Li R kun, Wei J yang, Wang L, Ma Y guang, Li Y hui. Restoration of infrared metalens images with deep learning. Opt Commun. 2024;552:130069.
[153] E. Tseng, S. Colburn, J. Whitehead, L. Huang, S.H. Baek, A. Majumdar, et al., Neural nano-optics for high-quality thin lens imaging, Nat. Commun. 12 (1) (2021) 6493.
[154] Y. Park, Y. Kim, C. Kim, G.Y. Lee, H. Choi, T. Choi, et al., End-to-End Optimization of Metalens for Broadband and Wide-Angle Imaging, Adv. Opt. Mater. 13 (9) (2025 Mar) 2402853.
[155] H. Zheng, Q. Liu, I.I. Kravchenko, X. Zhang, Y. Huo, J.G. Valentine, Multichannel meta-imagers for accelerating machine vision, Nat. Nanotechnol. 19 (4) (2024) 471–478.
[156] Colburn S, Zhan A, Majumdar A. Metasurface optics for full-color computational imaging. Sci Adv. 2025 Sep;4(2):eaar2114.
[157] M. Choi, J. Kim, S. Moon, K. Shin, S.W. Nam, Y. Park, et al., Roll-to-plate printable RGB achromatic metalens for wide-field-of-view holographic near-eye displays, Nat. Mater. 24 (4) (2025) 535–543.
[158] G.Y. Lee, J.Y. Hong, S. Hwang, S. Moon, H. Kang, S. Jeon, et al., Metasurface eyepiece for augmented reality, Nat. Commun. 9 (1) (2018) 4562.
[159] A. McClung, M. Torfeh, V.J. Einck, J.J. Watkins, A. Arbabi, Visible Metalenses with High focusing Efficiency Fabricated using Nanoimprint Lithography, Adv. Opt. Mater. 12 (9) (2024 Mar) 2301865.
[160] J. Seong, Y. Jeon, Y. Yang, T. Badloe, J. Rho, Cost-Effective and Environmentally Friendly Mass Manufacturing of Optical Metasurfaces Towards Practical applications and Commercialization, Int J Precis Eng Manuf Technol. 11 (2) (2024) 685–706.
[161] Y. Zhang, X. Jiang, G. Qu, J. Han, C. Li, B. Bo, et al., On-chip integration of achromatic metalens arrays, Nat. Commun. 16 (1) (2025) 7485.